J. Fluid Mech. (1981), *vol.* 105, *pp.* 283–316
Printed in Great Britain

The stability of vortices in a rotating, stratified fluid

By R. W. GRIFFITHS AND P. F. LINDEN
Department of Applied Mathematics and Theoretical Physics,
Silver Street, Cambridge

(Received 1 April 1980)

Axisymmetric flows with a two-layer density stratification are produced by releasing either a constant flux of fluid from a point source or a constant volume of fluid into a rotating environment with a different density. In both experiments the density interface intersects one horizontal boundary, forming a front. Transition to non-axisymmetric flow is observed and can be described by two parameters: θ, the square of the ratio of the internal Rossby radius of deformation to the horizontal length scale of the flow, and δ, the fraction of the total fluid depth occupied by the layer inside the front. For $\theta \ll 1$ and $\delta > 10^{-1}$ unstable disturbances obtain most of their energy from the potential energy of the flow, whilst for $\delta < 10^{-1}$ extraction of kinetic energy from the basic shear becomes the dominant driving mechanism. When the front intersects the free surface, $n = 2$ is the minimum azimuthal wavenumber for an unstable disturbance. At large amplitude of the growing waves, baroclinic and barotropic processes combine to form n vortex dipole structures which entrain buoyant fluid from the original vortex and propagate radially over the free surface. Vortices are also produced by the continuous release of fluid from a confined source at its own density level in a region of constant density gradient. As in the two-layer case the axisymmetric vortex grows to a critical size and then becomes unstable to a disturbance with wavenumber $n = 2$, producing, at large amplitude, two vortex pairs.

1. Introduction

There are a number of geophysically important situations in which surfaces of constant density, under the influence of the Coriolis force due to the Earth's rotation, intersect one horizontal boundary and in which the fluid motion is not constrained by rigid vertical walls. Isolated eddies, containing closed streamlines and with horizontal length scales of the order of 10^2 km, are found at the surface in many parts of the oceans. More rectilinear frontal zones between air or water masses of unequal density, intersecting the free surface of the ocean or the rigid bottom boundary of the atmosphere, also exist far away from vertical boundaries.

In this paper we discuss some laboratory experiments which elucidate a number of features of the stability of such flows. We concentrate upon vortices produced in a fluid with a two-layer stratification. The density interface between the layers intersects one horizontal boundary, either the free surface or the rigid bottom, far away from any vertical walls. Thus the streamlines of the flow are determined solely by the interaction of the Coriolis, centrifugal and buoyancy forces, and the influence of the upper and lower boundaries.

Two types of flow that satisfy the above conditions can readily be produced in the

laboratory. The first is similar to that observed by Saunders (1973). In his experiments a salt solution was placed inside a bottomless cylinder which was surrounded by a homogeneous layer of fresh water. After the system was brought to solid-body rotation, the cylinder was carefully removed. The denser fluid then collapsed and spread radially until it reached a state of quasi-geostrophic equilibrium (in which the radial pressure gradient due to buoyancy forces is balanced by the Coriolis and centrifugal forces). Under some conditions the resultant anticyclonic vortex remained stable and circular, but under other conditions it broke up into a well-defined number of smaller vortices. Saunders found that this behaviour could be described by a single dimensionless parameter $\theta_0 = g'h_0/f^2R_0^2$, where $g' = g\Delta\rho/\rho$ is the reduced gravity between the layers, h_0 is the initial depth of the denser salt solution (and also the total water depth), R_0 is the cylinder radius and $f = 2\Omega$ is the Coriolis parameter. When $\theta_0 > 1{\cdot}8$, the vortices were observed to be stable.

The second type of flow is produced when fluid is continuously supplied from a confined source region into an environment which has a different density and which is initially in solid-body rotation. In this case the vortex grows continuously both in depth and radius, and the anticyclonic motion in the vortex, which results from the radial motion of the fluid away from the source, always remains in a state of quasi-geostrophic balance. In the case with an infinitely deep environment Gil *et al.* (1979) found nonlinear solutions for both an inviscid vortex and for a vortex influenced by bottom friction. These authors also carried out some experiments in which dense fluid was forced through a small orifice onto the bottom of a container filled with less dense fluid in rigid rotation. The doming of the interface was only observed for a short time and the vortices were not observed to be unstable.

In this paper, we extend the study of both of these flows and make some attempts to relate the two. In § 3 we describe the flow produced by allowing a vertical cylinder of fluid to collapse toward an equilibrium state: a 'constant volume' experiment. In contrast to Saunders (1973) the fluid is less dense than the environment and so the vortex is formed at the free surface rather than on the bottom. In addition, the ratio $\delta_0 = h_0/H$ of the initial depth h_0 of fluid in the cylinder to the total depth H of the fluid was varied. We found that we could never produce a stable vortex, even for $\delta_0 = 1$ and θ_0 taking values at which Saunders' bottom vortices were stable. The smallest azimuthal wavenumber n of the unstable disturbances was $n = 2$. At a fixed value of θ_0, the wavenumber n first decreased as the depth ratio δ_0 was decreased from unity but reached a minimum at $\delta_0 \approx 0{\cdot}1$. At still smaller values of δ_0 the wavenumber increased again.

The vortices produced by the continuous release of fluid from a confined source in a rotating, homogeneous layer of finite depth H are described in § 4. These we will denote as 'constant flux' experiments. The axisymmetric vortices produced in this way were always observed to grow to a critical size at which they became unstable to a non-axisymmetric disturbance. For those vortices at the free surface, disturbances of azimuthal wavenumber $n = 2$ are the first to amplify.

Observations of the transition from axisymmetric to non-axisymmetric motion in the two types of vortices are complementary: the constant flux experiments allow a state of marginal stability to be approached slowly, whilst the constant volume experiments give rise to instability at supercritical conditions. Although the velocity and potential vorticity profiles are different in the two types of vortices, in both

systems the instabilities range from those that are almost purely baroclinic and driven by the release of potential energy, to those that are almost purely barotropic and which draw on the kinetic energy in the basic shear flow. The nature of the amplifying disturbances is similar in each type of vortex and the subsequent non-axisymmetric flows have several features in common. In particular, instability leads to a vortex-pairing behaviour which produces both splitting and rapid radial spreading of the vortex fluid. At an early stage of the pairing process cyclonic rings, or 'spiral arms', of buoyant fluid are produced.

In addition to the examples given earlier, there are a number of geophysical situations where isolated eddies and frontal regions are embedded within a fluid containing smooth density gradients. Experiments designed to investigate these flows are discussed in § 5, where we describe the flow that is produced by a continuous confined source of fluid embedded in a constant density gradient, far from horizontal boundaries. The resulting quasi-steady axisymmetric vortex is compared with steady solutions that were discussed recently by Gill (1981). This vortex is also found to become unstable and to break up in a manner similar to that for the two-layer case. Finally, in § 6 we present the main conclusions of this study and discuss the relationships between the constant volume and constant flux vortices.

2. The experiments

The experiments were performed on a 1 m diameter, direct-drive rotating turntable. In order to cover a range of fluid depths two cylindrical Perspex tanks were used: one 90 cm in diameter and 30 cm deep, and the other 29 cm in diameter and 92 cm deep. A third, rectangular tank measuring 45 cm by 60 cm in cross-section and 45 cm deep was used for many experiments, enabling side-view shadowgraph observations to be made. In each case the tank was centred on the vertical rotation axis of the table.

For the constant volume experiments, a (dyed) fluid of density ρ_1 was contained within a bottomless cylinder of radius R_0. The cylinder was centred on the axis of rotation and immersed to the required depth in the surrounding fluid of density ρ_2. The dyed fluid was added until it formed a layer of depth h_0 within the cylinder. In the general case, the cylinder contained two layers of fluid (see figure 1*a*) and there was no horizontal pressure gradient at its bottom. The whole system was then left to come to a state of solid-body rotation.

The experiment was initiated by the vertical withdrawal of the cylinder, which was done as carefully as possible in order to minimize any mixing between the two fluids. When $\rho_1 > \rho_2$, the dyed fluid formed a vortex on the bottom of the tank, whereas, when $\rho_1 < \rho_2$, a surface vortex was formed. Two values of the cylinder radius R_0 were used: 4·75 cm and 7·30 cm. The initial depth ratio covered the range $0{\cdot}03 \leqslant h_0/H \leqslant 1$, where H is the total fluid depth.

In the constant flux experiments (see figure 1*b*) fluid of density ρ_1 was added continuously from a confined source at the free surface (or at the bottom) of a layer of density ρ_2, which was initially in solid-body rotation. The source consisted of a small (1 cm diameter) sphere of foam rubber attached to the end of a vertical pipe (0·3 cm diameter). The source was fed under gravity from a reservoir, both being mounted on the rotating table. The flow-rate Q was monitored by a flowmeter and held constant

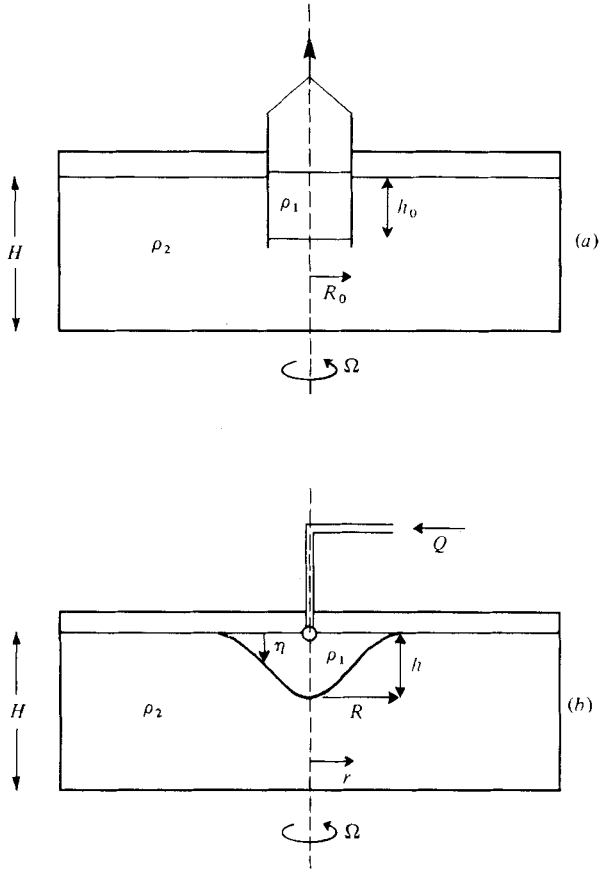

FIGURE 1. Diagrams showing the methods for producing two-layer vortices using (*a*) a constant volume initially constrained by a rigid cylinder and (*b*) a constant flux of fluid from a confined source area. In (*a*) the cylinder is shown in its position before being withdrawn. Symbols are defined in the text.

to within 10 % throughout a given experiment. The flow-rate took values throughout the range $0{\cdot}1 < Q < 3$ cm^3 s^{-1}.

In both experiments the density difference was produced by the addition of salt to one of the fluids. Consequently, the two fluids were miscible and mixing between them could occur. However, the amount of mixing was small and we shall treat the layers as though they were immiscible, but with no surface tension. The buoyancy forces are described by the parameter $g' = g|\rho_1 - \rho_2|/\rho_1$, where g is the gravitational acceleration. In the experiments g' varied from 0·1 cm s^{-2} to 10 cm s^{-2}. The Coriolis parameter f measured in radians per second was varied from 0·5 s^{-1} to 5·6 s^{-1}, and H from 10 cm to 90 cm. The only remaining extensive parameter was ν, the kinematic viscosity, but this was constant at 0·01 cm^2 s^{-1}.

The flows were visualized by the addition of dye, beads floating on the free surface, suspended aluminium particles and shadowgraph imagery. Plan-view photographs were taken in the rotating frame of reference, whose direction of rotation is anti-clockwise. All of the quantitative information presented in the following sections was obtained from the photographic record.

3. Constant-volume vortices

3.1. *Axisymmetric motion*

When both mixing and molecular diffusion between the two fluids are neglected, the axisymmetric flow produced by the gravitational collapse of a central cylinder of fluid is described by four dimensionless parameters. These are a Richardson number, $\theta_0 = g'h_0/f^2R_0^2$, the aspect ratio h_0/R_0 for the cylinder of buoyant fluid, the fractional depth $\delta_0 = h_0/H$ and an Ekman number $\nu/h_0^2 f$. The parameter θ_0 is the square of the ratio of the Rossby radius of deformation $(g'h_0)^{\frac{1}{2}}/f$ to the initial radius R_0 of the central cylinder. When $\theta_0 < 1$, the initial adjustment will produce an anticyclonic vortex with a maximum depth $h \lesssim h_0$, but h is much less than the initial depth when $\theta_0 \gg 1$. The ratio of vertical and horizontal length scales of the adjusted vortex is also determined by the initial aspect ratio, which was varied through the range $0{\cdot}2 < h_0/R_0 < 2$. The Ekman number describes the influence of friction at the density interface, the rigid bottom and the free surface. Since the Ekman number is of the order of 10^{-4} in the present experiments, we shall treat the axisymmetric flow as though it were inviscid. However, a comparison between vortices on the free surface and those on the bottom will show that this may not be a valid assumption when considering the stability of vortices adjacent to a rigid surface (see § 3.2).

The adjustment of the fluids after the retaining cylinder wall is removed is initially dominated by the buoyancy force. When $\rho_1 < \rho_2$, the less dense fluid rises and spreads radially at the surface. Conservation of angular momentum then implies that the spreading fluid must form an anticyclonic azimuthal flow. Similarly, fluid in the lower layer moves in towards the axis and forms a cyclonic flow. Radial motions are then opposed by a Coriolis force due to the azimuthal flow. The system rapidly adjusts (in a time of order f^{-1}) to a quasi-geostrophic equilibrium state in which buoyancy, Coriolis and centrifugal forces are balanced. As confirmed by Saunders (1973), the radius R of the vortex increases by approximately one Rossby radius, i.e.

$$R \doteq R_0(1+\theta_0^{\frac{1}{2}}).$$

As the radius increases the depth decreases, and both effects induce anticyclonic motion in the vortex. Similarly, both the radial inflow and the increase in depth induce cyclonic motion in the lower layer. The final depth and velocity profiles in the case of an infinitely deep bottom layer are discussed by Csanady (1979) and Flierl (1979). They show that the maximum azimuthal velocity occurs at the outer edge of the vortex and is of order $(g'h_0)^{\frac{1}{2}}$. When the bottom layer has a finite depth, the magnitude of the azimuthal velocity in the lower layer is zero at $r = 0$ and $r \approx R$, and passes through a maximum somewhere near $r \lesssim R_0$.

After adjustment the axisymmetric vortex still contains potential energy stored in the density field. This potential energy is a possible energy source for non-axisymmetric motions via baroclinic instability, and Saunders concluded that this was the source of energy for the instabilities he observed. On the other hand, the kinetic energy associated with the horizontal shear is a possible energy source for barotropic instabilities. It is known (see e.g. Gill, Green & Simmons 1974) that the energy source for instability in a two-layer flow depends on the relative depths of the layers, as well as on the potential and kinetic energy in the basic flow. In our experiments we investigate the transition to non-axisymmetric flow as a function of θ_0 and δ_0.

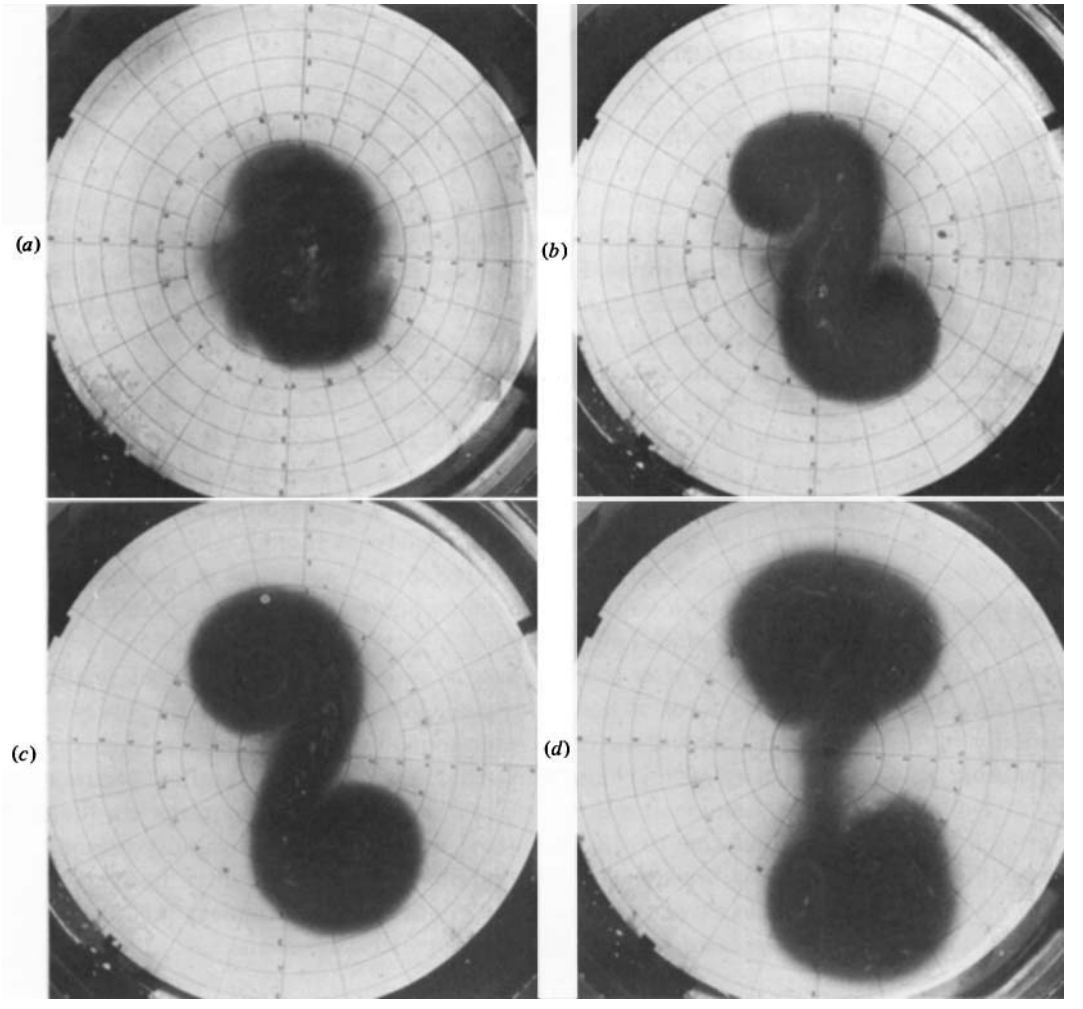

FIGURE 2. A sequence of plan-view photographs (taken in the rotating frame of reference) of a constant volume vortex that is unstable to a disturbance with $n = 2$. The frames were taken 2·3, 4, 7 and 10 revolutions after the cylinder was removed. The central anticyclonic circulation becomes elongated and then strong cyclonic motions with closed streamlines appear near each end. In frames (*b*) and (*c*), so much dyed fluid is entrained into cyclonic rings that it appears to spread over the radius of the cyclones. In frame (*d*), two dipole structures move away in opposite directions. Concentric circles on the base of the tank are at 4 cm intervals. The tank rotates in the anticlockwise direction. $f = 1{\cdot}45\ \mathrm{s}^{-1}$, $g' = 6\ \mathrm{cm\ s}^{-2}$, $H = 10{\cdot}7$ cm, $R_0 = 7{\cdot}3$ cm, $\theta_0 = 0{\cdot}31$, $\delta_0 = 1{\cdot}0$.

3.2. *Non-axisymmetric motion*

(i) *Onset of instability.* We restrict our attention to the case where the vortex is less dense than the environment and spreads out on the free surface. Most of the qualitative features are the same for the dense bottom vortices, and we will point out the few differences at the end of the section. Saunders gives results for bottom vortices with $\delta_0 = 1$ and our results for that case are in agreement with his.

Over the whole parameter range we were able to cover, we found that the axisymmetric motion was unstable to non-axisymmetric disturbances. These began to manifest themselves after a few (2 to 10) rotation periods as growing perturbations

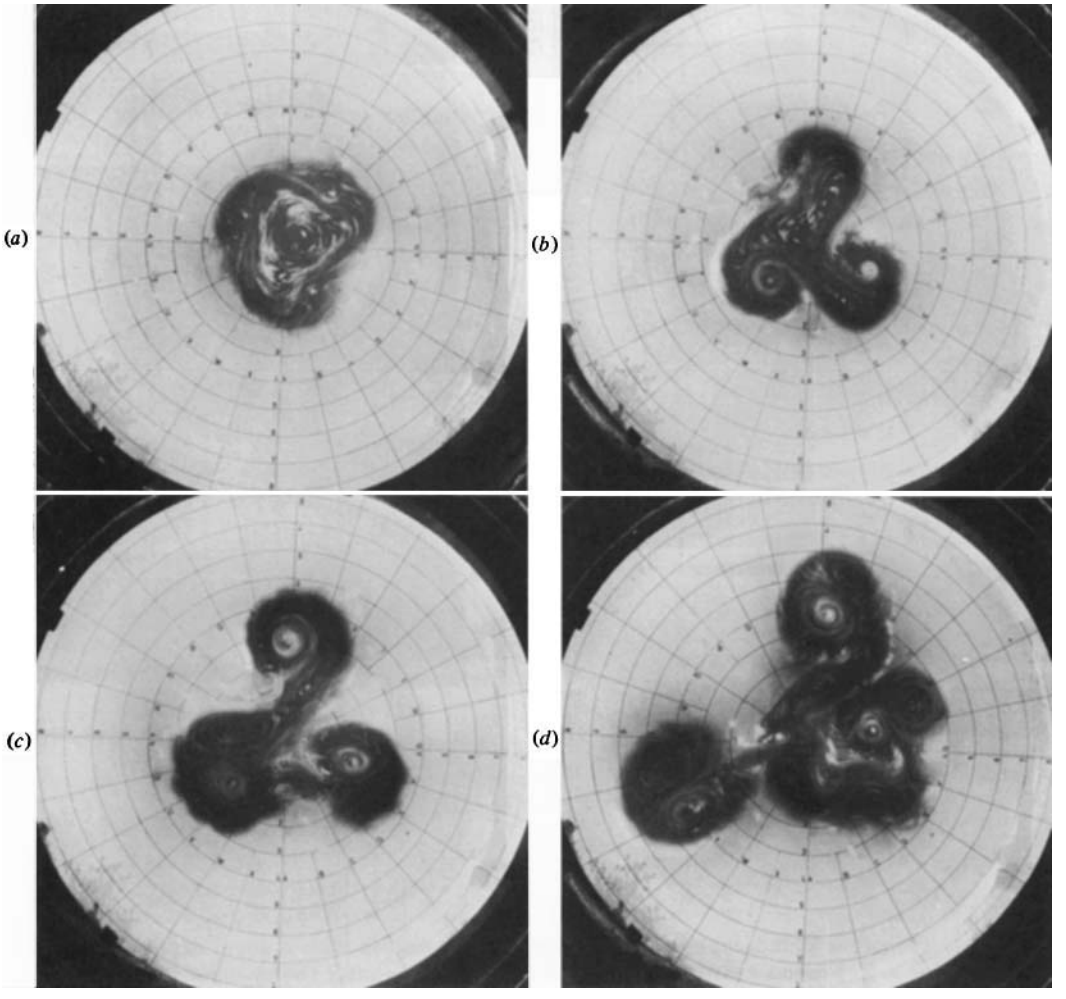

FIGURE 3. Plan-view photographs of a constant volume vortex with a large depth ratio showing an unstable disturbance with $n = 3$. Frames are at 5, 9, 11 and 12 revolutions after the cylinder was withdrawn. Much of the dyed fluid is entrained into the cyclonic rings in (*b*). Three vortex pairs are formed and these remove all of the dyed fluid from the original vortex. $f = 2{\cdot}82\ \mathrm{s}^{-1}$, $g' = 4{\cdot}5\ \mathrm{cm\ s}^{-2}$, $H = 12{\cdot}2$ cm, $R_0 = 7{\cdot}3$ cm, $\theta_0 = 0{\cdot}13$, $\delta_0 = 1{\cdot}0$.

to the initially circular shape of the vortex. The zonal wavenumber n of the perturbation was found to depend on θ_0 and δ_0, and took integer values $n \geqslant 2$. Examples of the onset and growth of these non-axisymmetric motions are illustrated by the three experiments shown in figures 2, 3 and 4. In figure 2 ($\theta_0 = 0{\cdot}31$, $\delta_0 = 1{\cdot}0$) an $n = 2$ disturbance amplifies, while in figures 3 ($\theta_0 = 0{\cdot}13$, $\delta_0 = 1{\cdot}0$) and 4 ($\theta_0 = 0{\cdot}092$, $\delta_0 = 0{\cdot}2$) the disturbance has wavenumber $n = 3$. We will consider the large amplitude behaviour of these instabilities later, but first we will examine some of the quantitative aspects of the initial perturbations.

The wavenumber n of the perturbation is plotted against θ_0 and δ_0 in figure 5. Only these two parameters are shown because no dependence of the form or behaviour of the disturbance upon h_0/R_0 was detected. For fixed δ_0 we see that n increases as θ_0 decreases, a result that was found for bottom vortices (with $\delta_0 = 1$) by Saunders.

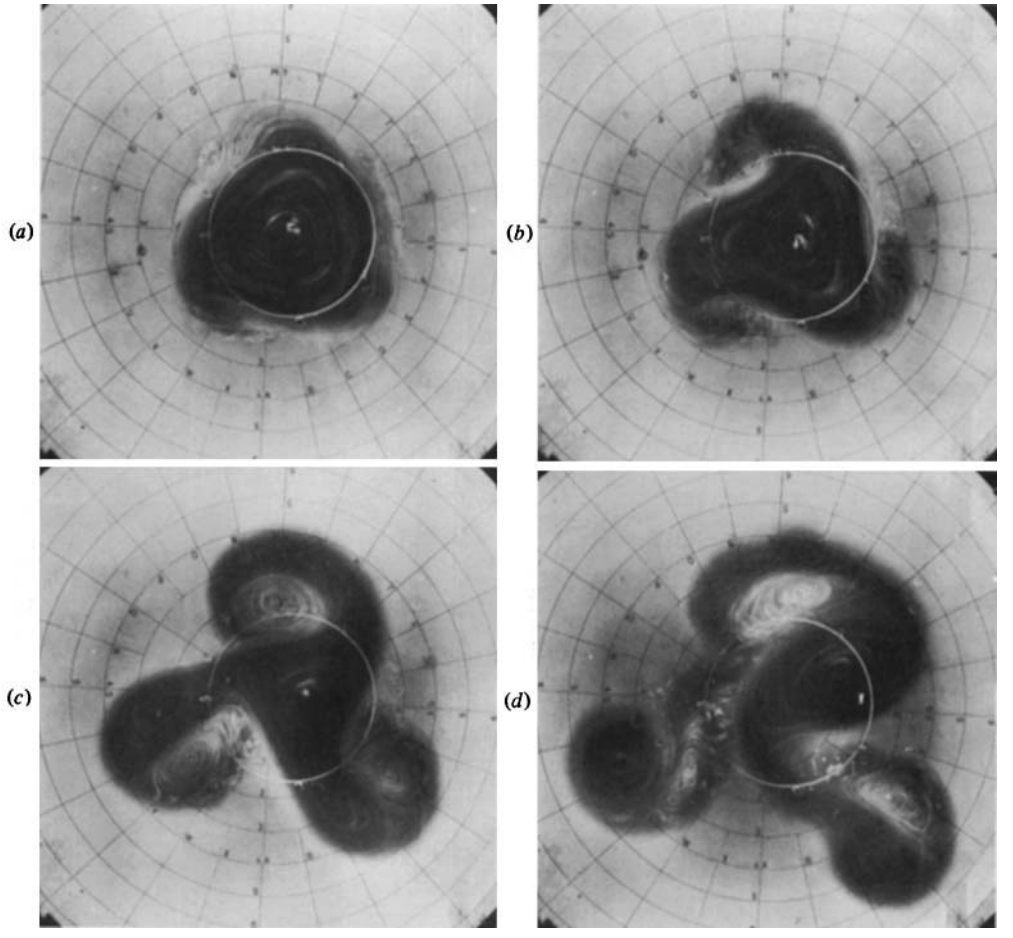

FIGURE 4. Plan-view photographs of a constant volume vortex with a small depth ratio and unstable to $n = 3$. Frames are at 9, 11, 16 and 19 revolutions after the cylinder was removed. Closed cyclonic circulation has not begun in (*a*). Frames (*b*) and (*c*) show that only a small amount of dyed fluid is carried into the cyclonic rings, and that the anticyclonic circulation in each lobe of the disturbance pinches off from the central vortex without drawing all of the buoyant fluid out of the original vortex. In (*d*) there remains a large anticyclone after the three vortex dipoles have broken away. Within each dipole the anticyclonic part contains most of the dyed fluid. $f = 2{\cdot}96\ \mathrm{s}^{-1}$, $g' = 7{\cdot}5\ \mathrm{cm\ s}^{-2}$, $H = 28$ cm, $R_0 = 7{\cdot}3$ cm, $\theta_0 = 0{\cdot}092$, $\delta_0 = 0{\cdot}20$. The hole in the lid guides the cylinder and appears off-axis because the camera is mounted slightly to one side.

For fixed θ_0, on the other hand, n first decreases with δ_0 and then increases again. We note that the results from experiments with $H = 90$ cm are consistent with those obtained with $H = 20$ cm at the same values of θ_0 and δ_0. However, for $\delta_0 = 0{\cdot}1$, say, the vortices in the two tanks are 9 cm and 2 cm deep, respectively, and the Ekman numbers based on h_0 differ by a factor of 20. This implies that frictional effects, at least in surface vortices, are probably not important. In order to explain the dependence of the wavenumber n on the Richardson number and depth ratio, we shall now examine the stability of the vortex to baroclinic and barotropic disturbances.

(ii) *Baroclinic instability.* The essential features of the instability can be investigated by appealing to the following highly simplified model, first discussed by Phillips

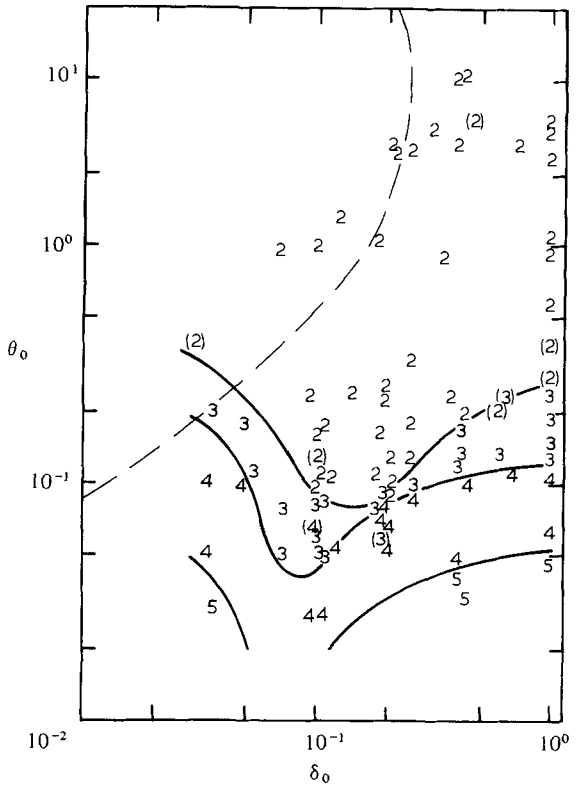

FIGURE 5. Observed values of the zonal wavenumber n as a function of the initial parameters θ_0 and δ_0. Solid lines are fitted by eye to the data and define transitions from one wavenumber to another. Numbers within brackets show experiments that could not be definitely classified. Modes with $n \geqslant 2$ are predicted to be baroclinically stable to the left of the broken line, which is given by (3.7).

(1954). Consider the two-layer flow of an inviscid fluid in an infinitely long, vertically sided channel between $y = 0$ and $y = R$, which is rotating about a vertical axis with rotation rate $\frac{1}{2}f$. The layers have uniform velocities U_1 and U_2 in the x direction. Phillips showed that, in the limit of very small Rossby number, but with $U_1 \neq U_2$, the flow is unstable to a disturbance with horizontal wavenumber K provided

$$K^2 < 2\left(\frac{\delta}{1-\delta}\right)^{\frac{1}{2}}\theta^{-1}. \tag{3.1}$$

Here we have defined $\theta = g'h/f^2R^2$ and $\delta = h/H$, where h is the depth of the upper layer and H is the total depth.

It is possible to write down the dispersion relation for this model. For a perturbation stream function of the form $e^{ik(x-ct)}\sin ly$, with $K^2 = k^2 + l^2$, the growth rate is given by

$$kc_i = k\frac{|U_1 - U_2|}{2}(1-\delta)^{\frac{1}{2}}\frac{[4\delta - K^4\theta^2(1-\delta)]^{\frac{1}{2}}}{1+K^2\theta(1-\delta)}, \tag{3.2}$$

where c_i is the imaginary part of the wave speed c. The wavenumber K and the phase speed c have been non-dimensionalized using the channel width R and the time scale

f^{-1}. By finding the stationary point of (3.2) it can be shown (when $\theta \ll \delta/[1-\delta]$) that the wavenumber k_m with the largest growth rate is given by

$$k_m \approx 0{\cdot}9\theta^{-\frac{1}{2}}\left(\frac{\delta}{1-\delta}\right)^{\frac{1}{4}}. \tag{3.3}$$

Before we can apply the results of the rectilinear problem to our axisymmetric laboratory flows, it is necessary to relate the values of θ and δ for the geostrophically adjusted vortex to the initial parameters θ_0 and δ_0 of the original cylindrical column (see figure 1). This can only be done quantitatively once the shape of the vortex is known, but the qualitative features of the relationships are not particularly sensitive to the exact shape. In order to illustrate the behaviour, we assume that the adjusted vortex has straight sides and that, when $\theta_0 \leqslant 1$, the depth η of the interface is given by

$$\eta(r) = \begin{cases} h, & 0 \leqslant r \leqslant R_0(1-\theta_0^{\frac{1}{2}}), \\ \frac{1}{2}h\theta_0^{-\frac{1}{2}}(1+\theta_0^{\frac{1}{2}})\,(1-r/R), & R_0(1-\theta_0^{\frac{1}{2}}) < r \leqslant R, \end{cases} \tag{3.4a}$$

where $R = R_0(1+\theta_0^{\frac{1}{2}})$ and h is the maximum depth after adjustment. When $\theta_0 > 1$, the sloping region of the interface extends all the way to the axis ($r = 0$) and we let

$$\eta(r) = h(1-r/R). \tag{3.4b}$$

Conservation of volume implies that

$$\frac{\delta}{\delta_0} = \begin{cases} (1+\frac{1}{3}\theta_0)^{-1}, & \theta_0 \leqslant 1, \\ 3(1+\theta_0^{\frac{1}{2}})^{-2}, & \theta_0 > 1, \end{cases} \tag{3.5a}$$

and

$$\frac{\theta}{\theta_0} = \begin{cases} (1+\frac{1}{3}\theta_0)^{-1}(1+\theta_0^{\frac{1}{2}})^{-2}, & \theta_0 \leqslant 1, \\ 3(1+\theta_0^{\frac{1}{2}})^{-4}, & \theta_0 > 1. \end{cases} \tag{3.5b}$$

Equation (3.5a) shows that, for fixed θ (or θ_0), increasing δ_0 is equivalent to increasing δ and that, when $\theta_0 < 1$, δ/δ_0 varies slowly with θ_0. On the other hand (3.5b) shows that θ increases like θ_0 for small θ_0, attains a maximum value of $\theta = 0{\cdot}188$ at $\theta_0 = 1$ and then decreases again like θ_0^{-1} for large θ_0. Using (3.5), the wavenumber of maximum growth rate predicted by (3.3) (now taking only integer values, n) becomes $n \sim \theta_0^{-\frac{1}{2}}[1+O(\theta_0^{\frac{1}{2}})]$ at $\theta_0 < 1-\delta_0 < 1$ and a fixed value of δ_0. This seems a reasonable approximation to the behaviour of the observed wavenumber provided that $\delta_0 > 0{\cdot}4$. Saunders (1973) reached a similar conclusion for bottom vortices with $\delta_0 = 1$. Furthermore, (3.3) predicts that a given wavenumber will be observed along a line $\theta \approx 0{\cdot}8k_m^{-2}(\delta/[1-\delta])^{\frac{1}{2}}$. With (3.5) our simple model gives $\theta_0 \sim n^{-2}(\delta_0/[1-\delta_0])^{\frac{1}{2}}$ at $\theta_0 \ll 1-\delta_0 < 1$, and $\theta_0[1+O(\theta_0^{\frac{1}{2}})] \sim n^{-\frac{4}{3}}\delta_0^{\frac{1}{3}}$ at $1-\delta_0 \ll \theta_0 < 1$. This behaviour, too, is very similar to that of the solid lines that mark the three transitions between wavenumbers on figure 5, provided that $\delta_0 > 0{\cdot}2$. Thus the properties of the observed disturbances at $\delta_0 > 0{\cdot}2$ are consistent with those of the baroclinically unstable disturbances predicted by Phillips' model. For $\delta_0 < 0{\cdot}1$, however, the wavenumber n is found to increase again as δ_0 is decreased further. We must seek an alternative explanation for this behaviour. First, though, we will find those conditions that give rise to marginally unstable baroclinic perturbations.

For baroclinic instability to occur (3.1), (3.5a) and (3.5b) show that we require

$$\frac{2}{\sqrt{3}}\frac{\delta_0^{\frac{1}{2}}}{K^2} > \begin{cases} \dfrac{\theta_0[\theta_0+3(1-\delta)]^{\frac{1}{2}}}{(\theta_0+3)\,(1+\theta_0^{\frac{1}{2}})^2}, & \theta_0 < 1, \\ \dfrac{\theta_0[(1+\theta_0^{\frac{1}{2}})^2-3\delta_0]^{\frac{1}{2}}}{(1+\theta_0^{\frac{1}{2}})^4}, & \theta_0 > 1. \end{cases} \tag{3.6}$$

The smallest unstable wavenumber observed in our experiments with surface vortices was $n = 2$. This corresponds to the value $K \simeq 2$ in (3.6) if the perimeter of the circular vortex is imagined to be a straight line. It will be explained below that only modes with $n \geqslant 2$ can grow. Given this result, (3.6) implies that stable vortices will only be found when

$$\frac{\delta_0^{\frac{1}{2}}}{2\sqrt{3}} < \begin{cases} \dfrac{\theta_0[\theta_0+3(1-\delta_0)]^{\frac{1}{2}}}{(\theta_0+3)\,(1+\theta_0^{\frac{1}{2}})^2}, & \theta_0 < 1, \\ \dfrac{\theta_0[(1+\theta_0^{\frac{1}{2}})^2-3\delta_0]^{\frac{1}{2}}}{(1+\theta_0^{\frac{1}{2}})^4}, & \theta_0 > 1. \end{cases} \tag{3.7}$$

This curve separating baroclinically stable and unstable vortices is shown on figure 5. There we see that for values of $\delta_0 > 0{\cdot}25$ (3.7) can never be satisfied and no stable vortices can be produced. On the other hand all vortices are stable in the limit as $\delta_0 \to 0$, a feature which is characteristic of baroclinic instability.

There are no stable vortices for $\delta_0 > 0{\cdot}25$ because, as mentioned above, θ attains a maximum as a function of θ_0. Hence increasing θ_0 in an attempt to produce a stable vortex merely leads to an adjusted vortex with a smaller value of θ.

It should be stressed that the comparison of the idealized baroclinic model of Phillips (1954) with our experiments is at best a qualitative one. It is well known that the conditions for baroclinic instability depend on the details of the velocity profile. However, the model assumes that there is uniform flow in each layer, whereas the vortices contain a strong radial velocity gradient. Furthermore, the model takes no account of the circular geometry, nor of the fact that the interface between the vortex and the environment intersects the free surface instead of rigid vertical walls. Even the depth profile we have assumed for the adjusted vortex is only an approximation to the real shape. Consequently, the curve representing marginal stability on figure 5 is shown only to give an idea of the qualitative behaviour of the system. Thus, although we believe that stable vortices cannot be found for values of δ_0 greater than some critical value, the value 0·25 given by (3.7) has little meaning. Unstable vortices are produced at conditions which satisfy (3.7), but it is impossible to say whether or not these conditions actually lie on the stable side of the appropriate marginal stability curve.

(iii) *Barotropic instability.* Phillips' model neglects another essential feature of the present experiments, namely the presence of horizontal shear. This can cause the vortex to be unstable to barotropic disturbances. Hide (1967) and Busse (1968) investigated the stability of the free shear layer produced by a differentially rotating disk in an unstratified, rotating fluid. They showed that instability occurs whenever the supply of kinetic energy from the shear is large enough to overcome the frictional dissipation, and that the wavenumber with maximum growth rate decreases as the thickness of the shear layer increases. The instability results in the production of a

regular pattern of vortices in the shear layer. In the present experiments the thickness of the shear layer is proportional to θ_0. Therefore, the wavenumber of the amplified barotropic modes should decrease with increasing θ_0.

The experimental results can now be interpreted in terms of mixed baroclinic and barotropic instabilities. In the limit as $\delta_0 \to 0$, only barotropic instability is possible (except at $\theta_0 \to 0$) while, at $\delta_0 \sim 1$, the instability is basically baroclinic and dominated by the release of potential energy. As δ_0 is decreased from unity (with fixed θ_0) the wavenumber of the baroclinic mode with the greatest growth rate decreases. The grow rate of that mode also decreases with δ_0, tending to zero at the curve of marginal stability for $n \geqslant 2$. Once δ_0 becomes small (say $\delta_0 \lesssim 0{\cdot}1$) the rate of supply of potential energy is overshadowed by the availability of kinetic energy from the horizontal shear. Because the wavenumber with maximum growth rate dominates the flow pattern, the wavenumber increases to the barotropic limit as $\delta_0 \to 0$. Thus the observed instabilities at $\delta_0 \sim 0{\cdot}1$ are of mixed type.

(iv) *The marginally unstable mode.* We now return to discussion of the minimum

geo-potential surface, a small motion of the vortex off the axis of rotation will lead to a centrifugal instability. In the case of a less dense vortex the centrifugal force tends to restore the vortex to its original position, so that $n = 1$ is not expected to grow for surface vortices.

3.3. *Large-amplitude behaviour*

The evolution of non-axisymmetric disturbances to very large amplitude is shown in the photographs of figures 2, 3 and 4 for wavenumber $n = 2$ and $n = 3$. The most striking feature of the flow is the formation of vortex pairs. The number of vortex pairs produced is equal to the wavenumber of the initial disturbance, and each pair consists of one cyclonic and one anticyclonic vortex. The relative motion of the vortex pairs causes the final break-up of the original vortex. In the following, the evolution of the flow, as a function of the depth ratio δ_0, is described.

We shall discuss the case $n = 3$, but the basic details are the same at all wavenumbers observed. As the photographs do not reveal the sign of the fluid velocity, the motion is sketched in figure 6. Figure 6(*a*) shows an anticyclonic vortex that is perturbed by a baroclinic $n = 3$ mode. At this small but finite amplitude of the wave, there is cyclonic vorticity about the points marked by crosses just ahead (in the anticlockwise direction) of each lobe of the disturbance. As the lobes grow in amplitude, closed cyclonic circulation is established about the crosses. This accumulation of cyclonic vorticity may be driven by the kinetic energy of the horizontal shear that is present near the density front. This point will be discussed further in § 6.

The new cyclonic vortices extend throughout the depth of the bottom layer and begin to entrain, at the surface, less dense fluid from the original vortex, as shown in figure 6(*b*). The entrainment produces rings of dyed fluid with cyclonic motion. The anticyclonic lobes eventually pinch off to form their own closed circulations. In contrast to the cyclonic rings, the resultant anticyclonic motion appears to be confined to the upper-layer fluid. The vortex pairs so formed continue to entrain fluid via narrow streams from the remaining central vortex, and they strengthen at its expense (figure 6*c*).

Until the vortex-pairing process is complete, the non-axisymmetric disturbances are stationary in the rotating frame of reference. This result is independent of wavenumber and differs from the observations of Saunders (1973). In his bottom vortices the pattern was advected in the direction of the flow. The difference may again be due to the different frictional effects caused by the bottom boundary and the free surface, but possibly also to a horizontal density gradient of opposite sign.

The relative strengths of the cyclones and anticyclones varies with the ratio of layer depths. This can be seen in figures 3 and 4, which show the $n = 3$ instability for $\delta_0 = 1{\cdot}0$ and $\delta_0 = 0{\cdot}20$, respectively. Although the initial perturbations are very similar in appearance, the cyclones are much less intense for small values of δ_0. Consequently the cyclones entrain much less dyed fluid from the original vortex. The closed circulations of the new anticyclones also contain less of the original upper-layer fluid than they do when $\delta_0 \approx 1$. Thus, in figure 4, the three vortex pairs move away (the anticyclones appearing strongest) leaving a smaller, but still vigorous, central anticyclonic vortex. In figure 3, almost all of the upper-layer fluid is carried away by the three vortex pairs, and this fluid is more nearly equally partitioned between the circulations of opposite sign.

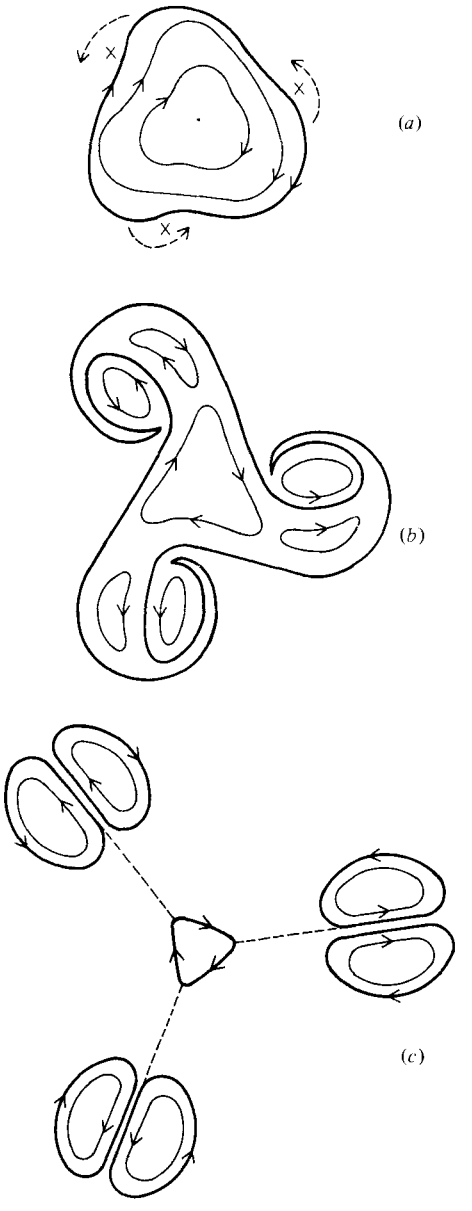

FIGURE 6. Schematic diagrams of the motion that is observed during the break-up, with $n = 3$, of a constant volume vortex. A depth ratio $\delta_0 \sim 0{\cdot}4$ is assumed, but the flow at larger values of δ_0 differs only in that more of the original vortex fluid is removed by the vortex dipoles and a greater proportion of the dyed fluid is found in the cyclones. In (*a*) the crosses mark the points about which cyclonic motion develops.

The qualitative observations of the large amplitude behaviour are consistent with a changing role of kinetic and potential energies as the depth ratio is varied. The cyclones formed at the edge of vortices with small δ_0 are similar to the shear-layer instabilities observed beneath a differentially rotating disk (Hide 1967). This barotropic process, through vortex pairing, assists the growth of a baroclinic mode of the same wavenumber and a small fraction of the potential energy stored in the original

vortex is released. On the other hand, when $\delta_0 \sim 1$, instability greatly reduces the potential energy of the flow, and the disturbance growth rate is several times greater.

We have not made a systematic study of the final stages of interaction between the vortex pairs. However, those formed from an $n = 2$ mode propagate radially in opposite directions under the influence of their own vorticity. This also appears to be true when $n = 3$ and δ_0 is not too small. At small δ_0, though, the vortex pairs are much weaker and often appear to be influenced by the other pairs and by the remaining anticyclonic vortex (see figure 4) until the whole flow field is eventually dissipated by friction. A very similar vortex-pairing behaviour is observed in the confined source experiments which are discussed in the following section.

4. Constant flux vortices

4.1. *Axisymmetric flow*

We now consider the flow produced by the continuous addition of fluid from a confined source at the free surface (or at the bottom boundary) of a homogeneous layer, as sketched on figure 1(*b*). The homogeneous layer, of depth H, is in solid-body rotation before the source is turned on at time $t = 0$. A first approximation to the resulting flow can be obtained by neglecting the effects of friction at the density interface, the free surface and the tank bottom.

(i) *Inviscid vortex.* The inviscid flow, both inside and outside the vortex, is governed by the principle of conservation of potential vorticity. Once the incoming fluid has spread radially over an area much greater than that of the source, the source may be regarded as a delta function at the origin (Gill *et al.* 1979). This implies that fluid enters the vortex with zero angular momentum. Conservation of angular momentum implies that the azimuthal velocity in the vortex, relative to the rotating frame, is

$$v_1 = -\tfrac{1}{2}fr. \tag{4.1}$$

The initial potential vorticity in the environment is f/H and its conservation implies that

$$\frac{f+\zeta_2}{H-\eta} = \frac{f}{H},$$

where ζ_2 is the relative vorticity in the environment and $\eta(r)$ is the depth of the vortex. Thus the azimuthal velocity in the environment is given by

$$\frac{dv_2}{dr} + \frac{v_2}{r} = -f\frac{\eta}{H}. \tag{4.2}$$

When the input flow-rate is small, the radial pressure gradient due to buoyancy forces must be balanced by the Coriolis and centrifugal forces. For a Boussinesq fluid under the hydrostatic approximation this implies that

$$f(v_1 - v_2) + \frac{v_1^2}{r} - \frac{v_2^2}{r} = g'\frac{d\eta}{dr}, \tag{4.3}$$

where g' is the reduced gravity between the layers. Provided the depth of the vortex is small ($\delta = h/H \ll 1$), then $v_2^2 \ll v_1^2$ and we can neglect the centrifugal force in the

environment. Then differentiating (4.2) to find $d\eta/dr$, and using (4.1) to substitute for v_1, (4.3) becomes

$$r^2\frac{d^2v_2}{dr^2}+r\frac{dv_2}{dr}-\left(1+\frac{r^2f^2}{g'H}\right)v_2=\frac{f^3r^3}{4g'H}. \tag{4.4}$$

The solution of (4.4) that is regular at the origin is

$$v_2=AI_1(r/\lambda)-\frac{fr}{4}, \tag{4.5}$$

where $\lambda=(g'H)^{\frac{1}{2}}/f$ is the Rossby radius of deformation for the environment and A is a constant to be determined by matching the flow at $r=R$, the radius of the vortex at the surface (see figure 1*b*).

The boundary condition at $r=R$ is determined as follows. Mass continuity implies that the flux across any cylindrical surface of radius $r\geqslant R$ in the environment is equal to the input flow-rate Q into the vortex. That is

$$Q=2\pi rHu, \tag{4.6}$$

where $u=u(r)$ is the radial velocity component. Hence the radial displacement of fluid initially at $r=r_0$ is given by

$$r^2-r_0^2=\frac{Qt}{\pi H}. \tag{4.7}$$

Angular momentum is conserved during this radial motion and so

$$v_Lr=\tfrac{1}{2}fr_0^2, \tag{4.8}$$

where v_L is the azimuthal velocity measured in the laboratory frame. Substituting for r_0^2 from (4.7) and subtracting the velocity of the rotating frame, we find that, for $r\geqslant R$,

$$v_2=-\frac{fQt}{2\pi Hr}. \tag{4.9}$$

Thus the boundary condition for (4.5) becomes

$$v_2=-\frac{fQt}{2\pi RH}\quad\text{at}\quad r=R. \tag{4.10}$$

In order to apply this boundary condition it is necessary to determine the volume of the vortex, Qt. This is done by finding $\eta(r)$ from (4.3) after substituting for v_1 and v_2 from (4.1) and (4.5), and then integrating the profile to find the volume. This procedure leads to the result that

$$A=\frac{\lambda f}{2I_0(R/\lambda)}. \tag{4.11}$$

We then use this value for A to calculate the shape and size of the vortex. We find that the depth of the vortex at time t is

$$\eta(r,t)=h(t)-\frac{H[I_0(r/\lambda)-1]}{2I_0(R/\lambda)}, \tag{4.12}$$

and that the maximum depth $h(t)$ occurs at $r=0$. The maximum radius of the vortex occurs at the surface ($\eta(R)=0$) and is related to the maximum depth by the equation

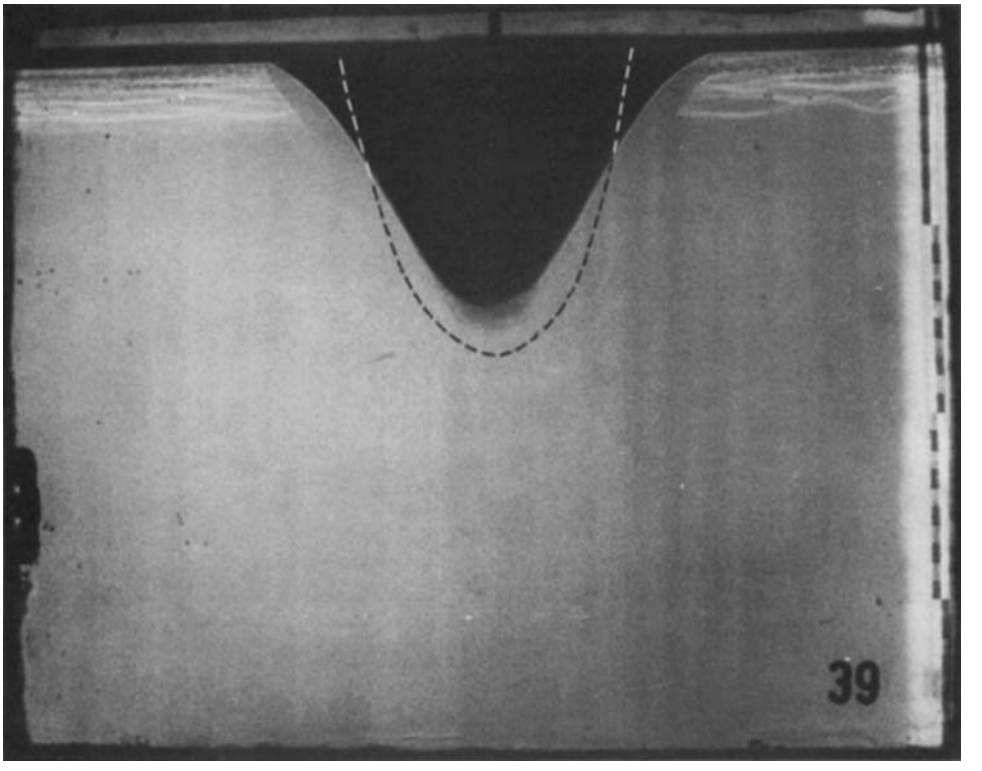

FIGURE 7. A shadowgraph showing a side view of a vortex produced by a constant flux of dyed fluid from a confined source. The profile given by (4.12) is superimposed. $f = 2{\cdot}4\ \mathrm{s}^{-1}$, $g' = 1{\cdot}0\ \mathrm{cm\ s}^{-2}$, $Q = 3{\cdot}0\ \mathrm{cm}^3\ \mathrm{s}^{-1}$, $H = 40$ cm, $\delta = 0{\cdot}32$ and $t = 570$ s. The scale on the right-hand side is in cm and offset every 10 cm.

$$h(t) = \frac{H[I_0(R/\lambda) - 1]}{2I_0(R/\lambda)}. \tag{4.13}$$

The volume of the vortex at time t is given by

$$Qt = \tfrac{1}{2}\pi R^2 H\left[1 - \frac{2\lambda I_1(R/\lambda)}{RI_0(R/\lambda)}\right]. \tag{4.14}$$

The shape of the vortex given by (4.12) is compared with a laboratory vortex on figure 7. For this case the depth ratio is $\delta = 0{\cdot}32$, the Rossby radius is $\lambda = 2{\cdot}64$ cm, and the radius $R\,(= 7{\cdot}75$ cm) is determined by substituting a known value for the volume Qt in (4.14). The theoretical curve gives a reasonable description of the observed interface shape, although the laboratory vortex has a greater radius and is shallower than predicted.

It is difficult to extract the explicit behaviour of the radius R and the maximum depth h with time from (4.13) and (4.14). However, in the limit $\delta = h/H \ll 1$ we can use series expansions of I_0 and I_1 to obtain

$$\hat{R}(\hat{t}) \simeq \frac{2}{\pi^{\frac{1}{4}}}\hat{t}^{\frac{1}{4}} \tag{4.15}$$

and

$$\hat{h}(\hat{t}) \simeq \frac{1}{2\pi^{\frac{1}{2}}}\hat{t}^{\frac{1}{2}}, \tag{4.16}$$

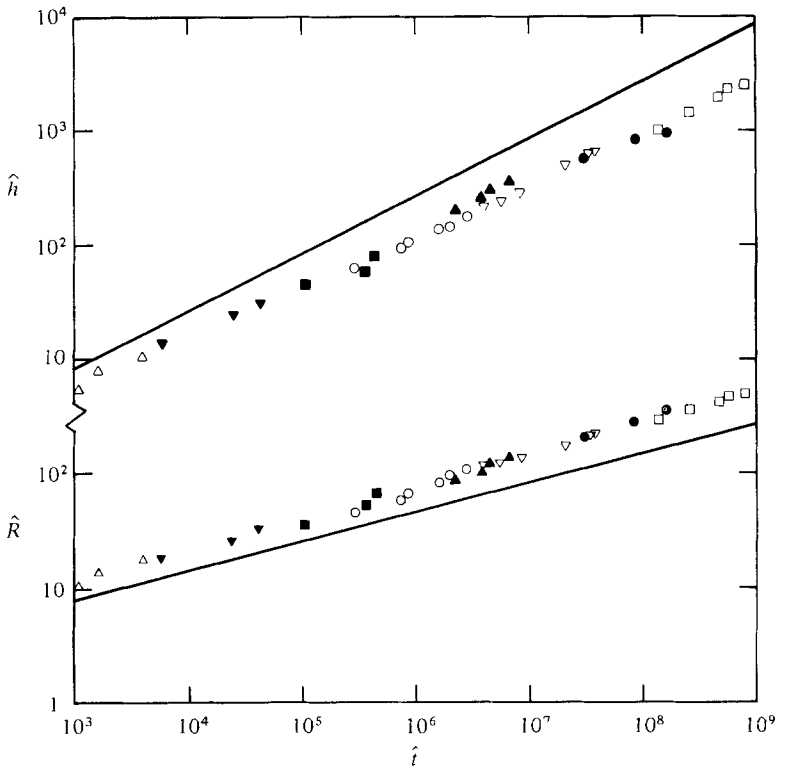

FIGURE 8. The dimensionless radius $\hat{R}$ and maximum depth $\hat{h}$ as functions of the dimensionless time $\hat{t}$, for a number of constant flux experiments. Eight experiments are shown, with $1 < f < 5\,\mathrm{s}^{-1}$, $0{\cdot}20 < g' < 10\,\mathrm{cm\,s}^{-2}$ and $0{\cdot}33 < Q < 3{\cdot}1\,\mathrm{cm}^3\,\mathrm{s}^{-1}$. The solid lines are those given by the inviscid model (4.15) and (4.16).

where the dimensionless radius and depth are given by $\hat{R} = f^2R/g'$ and $\hat{h} = f^2h/g'$, respectively, and the dimensionless time is $\hat{t} = Qf^6t/g'^3$. The radius and depth of a number of laboratory vortices are plotted against time on figure 8. The straight lines are those given by (4.15) and (4.16). The radius is found to increase approximately as $t^{\frac{1}{4}}$, while the depth increases as $t^{\frac{1}{2}}$. However the radius is 50–100 % greater and the depth 30–70 % smaller than predicted. There are a number of properties of the laboratory flow that have been neglected in the analysis and which contribute to this discrepancy. It was assumed that the source acts as a delta function at the origin whereas in fact it has a finite size. The fluid entering the vortex therefore has some cyclonic angular momentum, and its anticyclonic azimuthal velocity due to radial spreading is less than that given by (4.1). In addition, the neglect of the centrifugal force in the lower layer becomes a poor approximation as the depth ratio increases. Both of these effects imply that the slope of the interface should be less than predicted by (4.12). Finally, we have assumed that the motion is inviscid. We shall now briefly consider the effects of finite fluid viscosity on the vortex.

(ii) *Influence of friction.* In the experiments, Ekman boundary layers are produced on the free surface, on the rigid bottom and on the interface between the two layers. An Ekman number based on the maximum depth of the vortex takes values of $O(10^{-4})$ so that the Ekman layers are thin compared with the depth of the vortex.

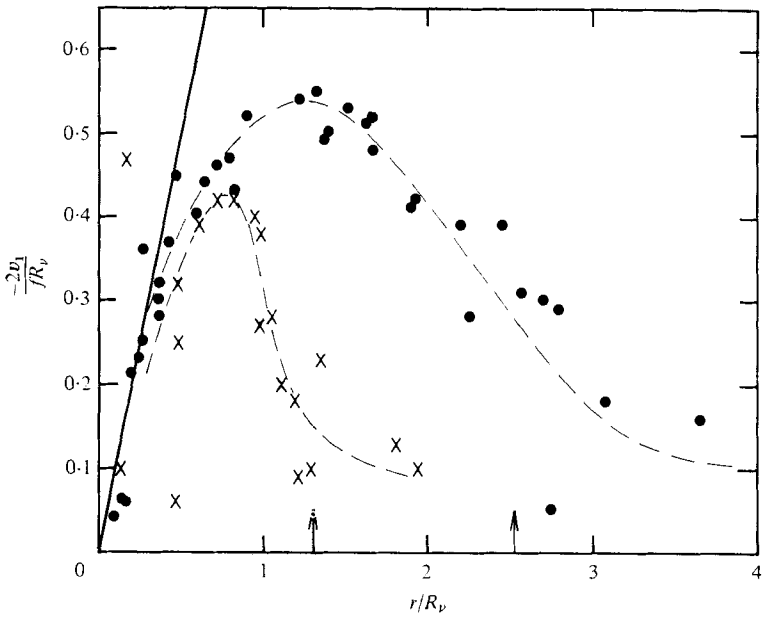

FIGURE 9. The radial profile of azimuthal velocity v_1 (1 cm to 3 cm below the surface) for an axisymmetric vortex at two stages during a single constant flux experiment: ×, t = 430 s; ●, t = 2990 s after the source flow began. The radius is non-dimensionalized by the viscous length scale R_ν given by (4.17). In this case R_ν = 3·1 cm. Arrows show the radius R of the vortex, the smaller value corresponding to the earlier time. The straight solid line is the velocity profile predicted for the upper layer by (4.1), and the two broken lines are fitted by eye to the data.

However, the associated Ekman transport can significantly alter the flow velocities and hence the shape of the density interface. Fluid in the outward-moving Ekman layers acquires angular momentum. Thus, as can be seen in figure 7, the slope of the interface required to balance the Coriolis force $f(v_1 - v_2)$ is smaller at larger radii and the vortex has a greater radial extent than that predicted by the inviscid analysis.

The flow within the vortex was visualized by adding dye to the source reservoir after the vortex had grown for some time. Fluid entering the vortex from the source first moves down along the axis of rotation in a column with a diameter roughly equal to that of the source. After reaching the tip of the vortex, the fluid is transported towards the outer edge of the vortex in the interfacial Ekman layer. The central vertical column of dyed fluid slowly enlarges in diameter, indicating the presence of a small radial velocity throughout the vortex. In the lower layer, fluid is carried in towards the tip of the vortex in an Ekman layer immediately below the interface. There is a very small amount of mixing between the fluids in the Ekman layers on either side of the interface, and this leads to the presence of mixed fluid beneath the tip of the vortex shown in figure 7.

The effect of the Ekman layers on the vortex is to spin up the fluid as it moves radially outward. Near the axis the fluid is not influenced by friction. This process can be characterized by a radial length scale R_ν at which the time scale for advection, R_ν/u_ν, equals the spin-up time scale $h_\nu/(f\nu)^{\frac{1}{2}}$, where u_ν and h_ν are suitable velocity and depth scales, respectively. From conservation of volume we also know that

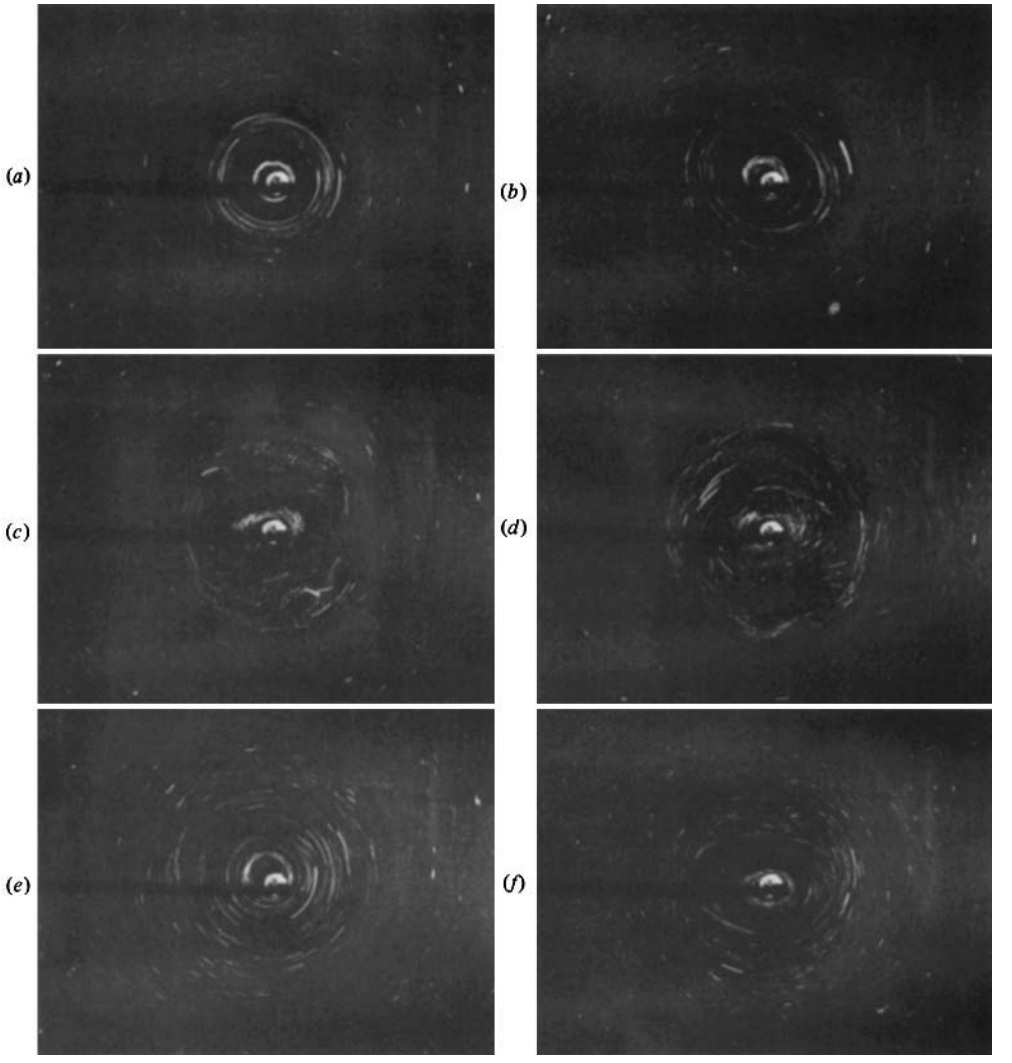

FIGURE 10. (*a–f*) For legend see opposite.

$Q = h_v R_v u_v$. It follows, as shown by Gill *et al.* (1979), that

$$R_v = Q^{\frac{1}{2}}(f\nu)^{-\frac{1}{4}}. \tag{4.17}$$

Gill *et al.* present numerical solutions for the flow in a dense vortex with bottom friction when the environment is stationary (infinitely deep). These show that the vortex has an essentially inviscid core of radius R_v inside which the depth and velocity profiles are close to those predicted by the inviscid model. When $R > R_v$, the azimuthal velocity has a maximum value near $r = R_v$ and then decreases to zero at both $r = 0$ and $r = R$.

In our experiments the radial profile of azimuthal velocity was determined from streak photographs of aluminium particles. Figure 9 shows velocity profiles (obtained from streaks in a horizontal sheet 1 cm below the free surface) for the axisymmetric flow at two times during one constant flux experiment. In this case the viscous length scale is $R_v = 3{\cdot}1$ cm and the vortex radius is given by $R/R_v = 1{\cdot}3$ (crosses) and

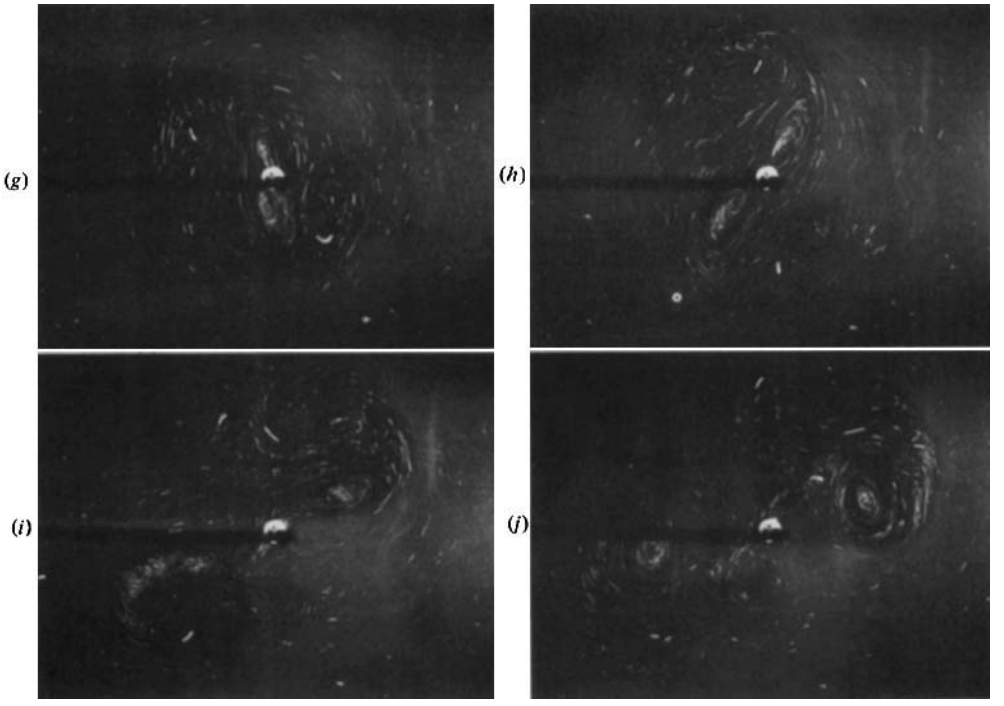

FIGURE 10. A sequence of streak photographs for one constant flux experiment, in which the source flow was turned off at $t = 2478$ s. The streaks are in a horizontal plane 1 cm to 3 cm below the free surface, and are 4 s exposures of aluminium particles suspended in the flow. Each frame shows an area 45 × 33 cm at the free surface. The frames are shown sequentially and were taken at the following times. (*a*) $t = 1246$ s; (*b*) $t = 1556$ s; (*c*) $t = 1610$ s; (*d*) $t = 1637$ s; (*e*) $t = 2003$ s; (*f*) $t = 2735$ s; (*g*) $t = 2743$ s; (*h*) $t = 2770$ s; (*i*) $t = 2800$ s; (*j*) $t = 2817$ s. The experimental parameters are $f = 2{\cdot}2\ \mathrm{s}^{-1}$, $g' = 0{\cdot}2\ \mathrm{cm\ s}^{-2}$, $Q = 1{\cdot}1\ \mathrm{cm}^3\ \mathrm{s}^{-1}$, $H = 40$ cm.

$R/R_\nu = 2{\cdot}5$ (circles). The velocity is normalized by the value $-\frac{1}{2}fR_\nu$ and the solid line is the velocity profile of the upper layer given by the inviscid theory for a point source. As the vortex enlarges, the velocity reaches a maximum near $r = R_\nu$ and decreases toward $v_2 (\neq 0)$ at $r \approx R$. The maximum velocity is significantly less than that predicted by (4.1) because of friction and the finite size of the source. At $r > R$ the lower layer moves anticyclonically as predicted by (4.9) but has also lost some angular momentum due to friction at the bottom of the tank.

4.2. *Non-axisymmetric flow*

(i) *Qualitative behaviour.* We have described the basic axisymmetric, two-layer flow that is produced by a confined source of fluid. However, all of the observed vortices reached a stage at which the flow became non-axisymmetric. The qualitative nature of the transition to non-axisymmetric flow and the subsequent motions will be described here by reference to the experiment shown in figure 10. This sequence of plan-view streak photographs shows the motion in a plane 1 to 3 cm below the free surface for this vortex. The source flow was begun at time $t = 0$, and the subsequent times are given for each frame. The dark shadow to the left of the vortex is a shadow produced by dye in the source fluid, and its size indicates the diameter of the vortex at the surface.

Initially the anticyclonic flow is circular and stable, as shown in the first frame. A disturbance of azimuthal wavenumber $n = 2$ then becomes visible (*b*). The subsequent behaviour of the disturbance is very similar to the $n = 2$ instabilities of the constant volume vortices described in § 3.2. Two 'arms' of source fluid grow from the outer extremities of the disturbance and these arms are wound into cyclonic eddies, one on each side of the elongated central vortex (*c*). During this process the whole pattern drifts anticyclonically (in contrast to the constant volume vortices for which the disturbance is stationary in the rotating frame) due to the motion in the lower layer (see (4.9)).

After the development of the two cyclonic eddies, the evolution of the flow follows one of two paths. Sometimes, an instability with a smaller length scale appears in the flow, accompanied by the dissipation of the cyclonic eddies. This stage is seen in figure 10(*d*). Provided the source flow is maintained, a stable, circular vortex is re-established (*e*) and the cyclonic eddies are engulfed by the central vortex as it continues to grow. This vortex eventually becomes unstable again (*f*), with the instability taking the same form as the first instability. This second instability may also decay to produce yet another axisymmetric vortex. We have observed a sequence of as many as three such transitions from axisymmetric to non-axisymmetric flow in a given experiment. The smaller scale instability is always observed before the redevelopment of a stable circular vortex from a non-axisymmetric flow. The nature of the process is not known. It might extract energy from the velocity shear via the Kelvin–Helmholtz mechanism or it might extract potential energy from the density field via the super-critical, baroclinic, finger-like cells discussed by Pedlosky (1976).

An alternative evolution of the flow after the growth of an $n = 2$ disturbance and the formation of two cyclonic eddies is that shown in figure 10(*f*) to (*j*). The central vortex becomes increasingly eccentric (*g*) until it separates into two distinct anticyclonic eddies (*h*). There are then two vortex pairs each containing one cyclonic and one anticyclonic eddy. This behaviour is identical with that observed in the constant volume experiments. The two anticyclones are again connected by a narrow, high-velocity stream that contains flow in opposite directions on the two sides (*i* and *j*). The two vortex pairs travel radially in opposite directions and the narrow jet eventually breaks. No input fluid is left at the source.

In the example shown in figure 10 the source was turned off before the beginning of the second instability. However, a similar break-up of the central vortex also occurs when the source flow is maintained, as in figure 11. The only noticeable difference is that when the source is left on the cyclones are less intense, and the anticyclones more intense.

Observations from the side show further features of the transition from circular to non-axisymmetric flow. Shadowgraph side-views of the transition for one laboratory vortex are shown in figure 12, and the corresponding plan views (using dyed source fluid) are shown in figure 13. The stable, circular flow is shown in (*a*) and (*b*) of each figure. The early stages in the formation of the two 'spiral arms' are shown in (*c*) of each figure. At this stage irregularities, or kinks, have appeared on the density interface. The deep anticyclone is elongated by the $n = 2$ disturbance and (*d*) and (*e*) show the major and minor axes of the vortex, respectively.

Although it is not readily apparent from these still photographs, we observed that, during the early stages of the transition, the azimuthal disturbance has a depth-dependent structure. It was particularly noticeable on deeper vortices, but seems to

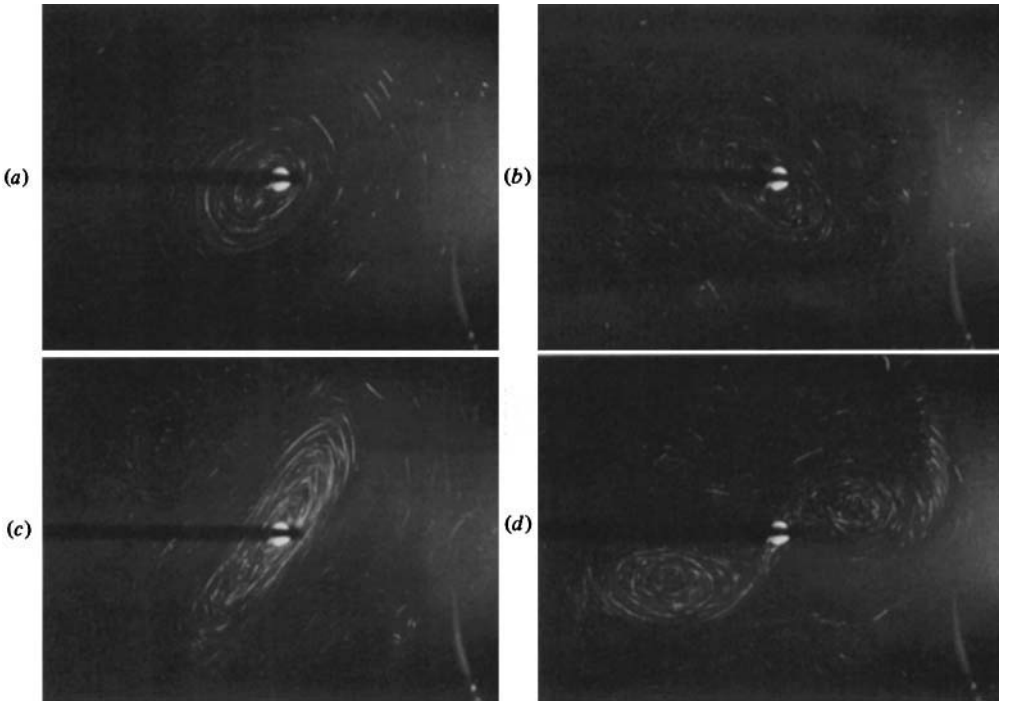

FIGURE 11. A sequence of streak photographs of an experiment similar to that shown in figure 10, except that here the source flow is maintained throughout. The frames were taken at the following times. (*a*) $t = 3420$ s; (*b*) $t = 3480$ s; (*c*) $t = 3540$ s; (*d*) $t = 3570$ s. The experimental parameters are $f = 1{\cdot}1\ \mathrm{s}^{-1}$, $g' = 0{\cdot}2\ \mathrm{cm\ s}^{-2}$, $Q = 1{\cdot}0\ \mathrm{cm}^3\ \mathrm{s}^{-1}$, $H = 40$ cm.

be common to all the vortices. The elongated vortex is twisted around in the anticyclonic direction with increasing depth. This implies that the phase of the azimuthally propagating wave increases with depth. Such a phase variation is a distinguishing feature of baroclinically unstable disturbances (Gill *et al.* 1974) and suggests that the kinetic energy of the disturbance is provided by the release of potential energy from the density field.

Figures 12(*f*) and 13(*f*) show that the 'spiral arms' continue to develop and that they carry the less dense fluid outward into the cyclonic eddies. The central vortex is consequently reduced in depth, as shown by the shadowgraphs (*e*) and (*f*). Thus the instability enables the fluid in the vortex to overcome the rotational constraint. The fluid spreads radially and reduces the potential energy of the flow.

We have only discussed those experiments in which the non-axisymmetric disturbances had an azimuthal wavenumber $n = 2$. No examples were found of vortices which remained stable ($n = 0$), or which became unstable at higher wavenumbers ($n \geqslant 3$). The only exceptions to $n = 2$ were a few cases where the vortex wandered off the source, a behaviour that may be regarded as an amplification of an $n = 1$ baroclinic mode. This occurred at high values of the rotation rate ($f > 4\ \mathrm{s}^{-1}$), where the curvature of the free surface was pronounced and may have influenced the vortex motion. Some experiments were also performed with the source on a rigid horizontal base. Dense fluid supplied from the source then produced an inverted vortex on the bottom. In this case all vortices wandered off the source. This behaviour is probably

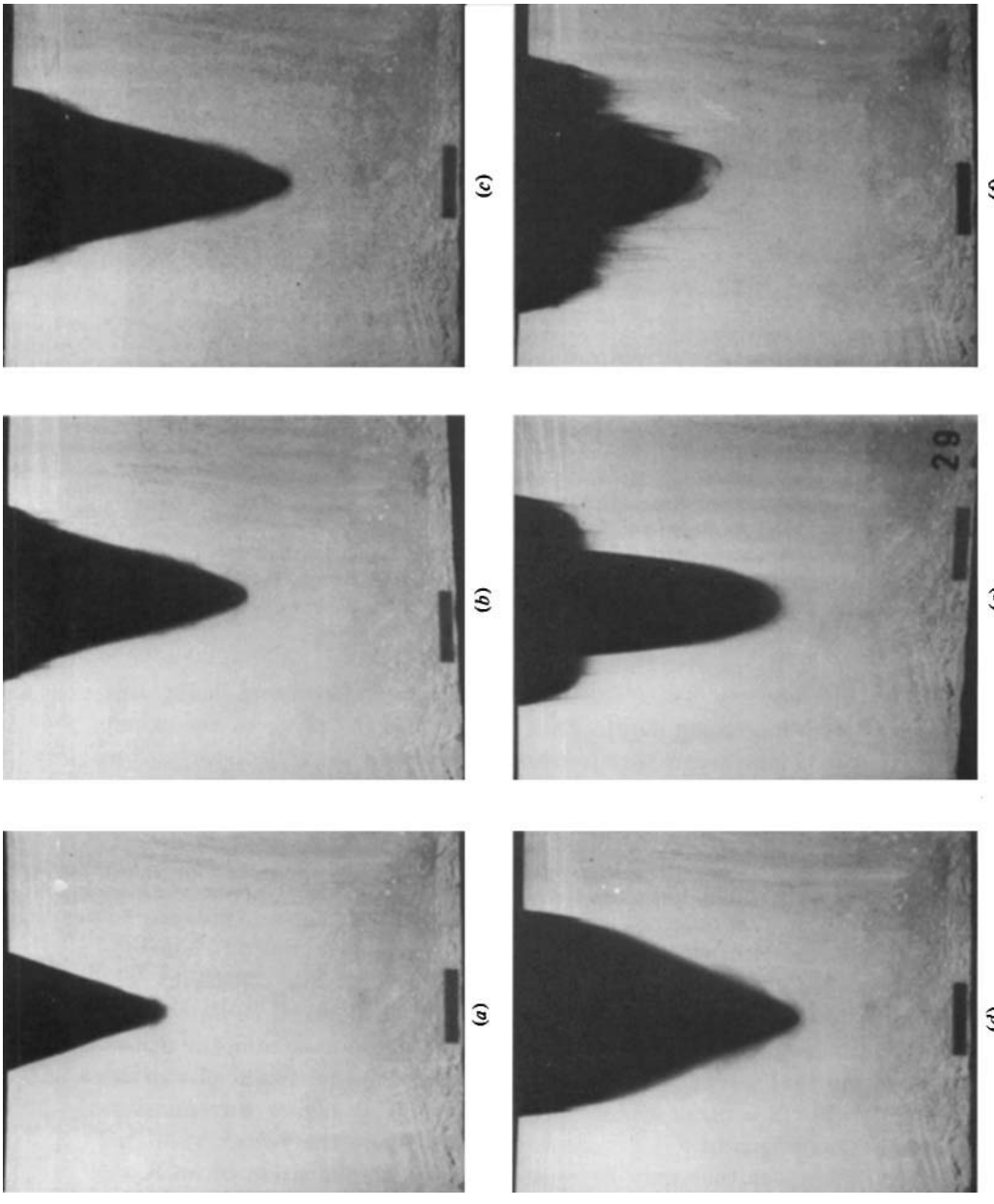

FIGURE 12. A sequence of side-view shadowgraphs showing the evolution of the vortex for one constant flux experiment with $f = 2{\cdot}74\ \mathrm{s}^{-1}$, $g' = 0{\cdot}2\ \mathrm{cm\ s}^{-2}$, $Q = 0{\cdot}71\ \mathrm{cm}^3\ \mathrm{s}^{-1}$ and $H = 40$ cm. The source began at $t = 0$ and the frames are at the following (approximate) times: (*a*) $t = 515$ s; (*b*) $t = 1980$ s; (*c*) $t = 2010$ s; (*d*) $t = 2030$ s; (*e*) $t = 2080$ s; (*f*) $t = 2100$ s. The tape near the bottom of the tank is 5 cm long.

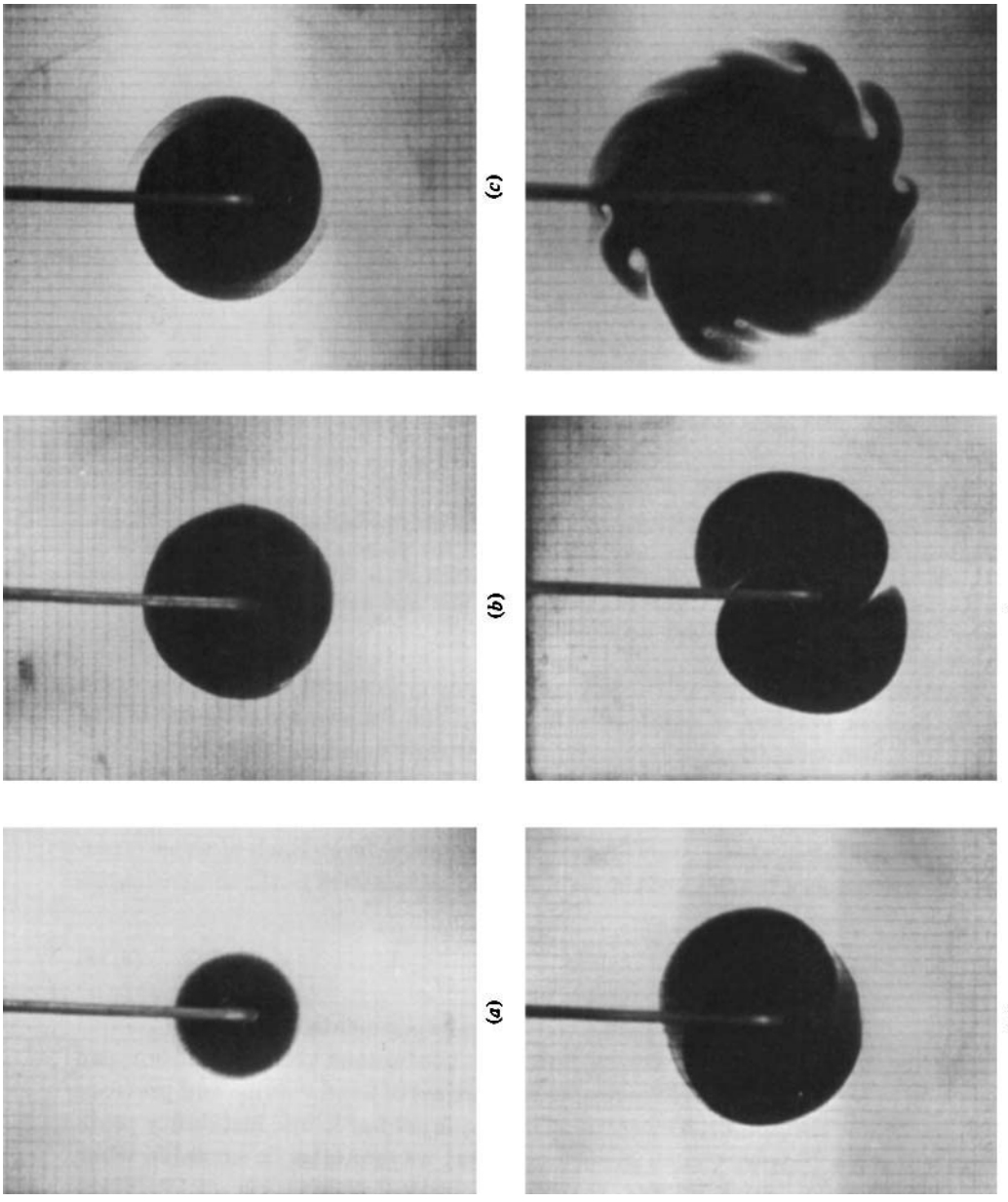

FIGURE 13. A sequence of plan-views for the same experiment as shown in figure 12. The (approximate) times for the frames are (*a*) $t = 870$ s; (*b*) $t = 1980$ s; (*c*) $t = 2010$ s; (*d*) $t = 2030$ s; (*e*) $t = 2080$ s; (*f*) $t = 2100$ s. The grid is in 1·14 cm squares.

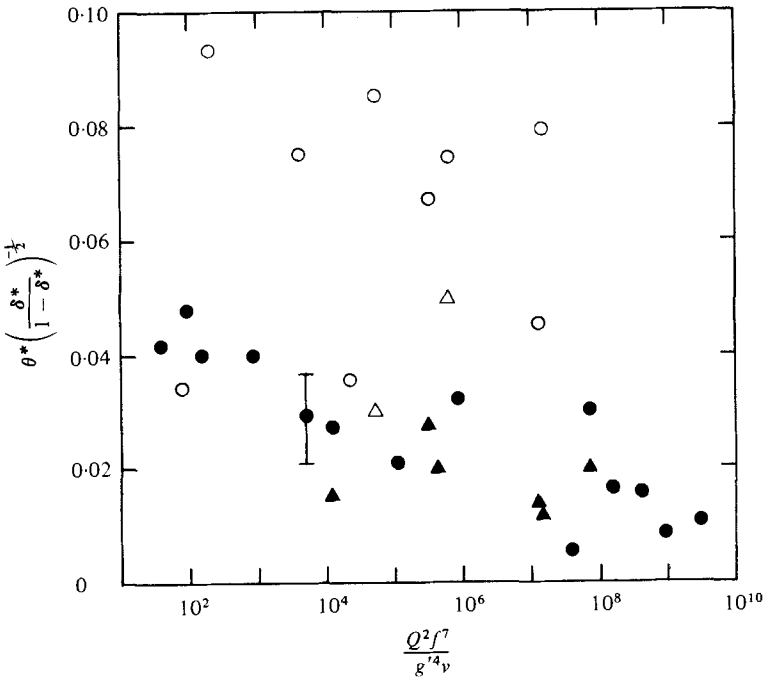

FIGURE 14. The value of $\theta^*(\delta^*/[1-\delta^*])^{-\frac{1}{2}}$ measured immediately prior to the onset of instability for the constant flux vortices, as a function of the ratio of the viscous to advective time scales $\phi = Q^2f^7/g'^4\nu$. The closed symbols refer to vortices for which $\delta^* > 0{\cdot}2$, and the open symbols to those with $\delta^* < 0{\cdot}2$. Circles and triangles denote the first and subsequent instabilities of a vortex, respectively. Typical error bars are shown.

due to a centrifugal instability of the horizontal density gradient, as was discussed in § 3.2 for bottom vortices of constant volume. In the following discussion of the conditions at which transition to non-axisymmetric flow occurred, only those cases in which disturbances had a wavenumber $n = 2$ will be considered.

(ii) *Critical conditions.* Measurements of the radius R^* and the maximum depth h^* of the vortex were taken at the onset of non-axisymmetric flow. Each of these quantities can be written as a function of the independent parameters in the dimensionless form

$$\frac{f^2R^*}{g'}, \frac{f^2h^*}{g'} = \mathscr{F}\left(\frac{f^2H}{g'}, \frac{Qf^5}{g'^3}, \frac{Q^2f^7}{g'^4\nu}\right). \tag{4.18}$$

Only the kinematic viscosity ν was held fixed in our experiments.

The stability of the laboratory vortex flow with continuous volume addition can be understood in terms of the stability results for vortices of fixed volume and previous studies of baroclinic instability. The rectilinear, two-layer baroclinic instability problem discussed in § 3.2 shows that a given horizontal wavenumber is unstable when the parameter $\theta(\delta/(1-\delta))^{-\frac{1}{2}}$ is less than some critical value (see (3.1)). Here $\theta = g'h/f^2R^2$ is again an internal Richardson number for the vortex and $\delta = h/H$ is the depth ratio. As noted in § 3.2, a similar result was found by Hart (1972, 1980) for two-layer flow with circular geometry.

The value of θ and δ at the time that disturbances begin to grow will be denoted by θ^* and δ^* respectively. In figure 14 the laboratory data for $\theta^*(\delta^*/(1-\delta^*))^{-\frac{1}{2}}$ are

plotted against $\phi = Q^2 f^7/g'^4\nu$, which is the ratio of the time scale $(fQ/g'\nu)$ required for Ekman pumping to spin up the vortex and the time scale (g'^3/Qf^6) required for inviscid radial advection. As a given vortex grows, the value of θ slowly decreases, while $\delta/(1-\delta)$ increases. Therefore, during the growth of a stable, circular vortex, the value of $\theta(\delta/(1-\delta))^{-\frac{1}{2}}$ decreases with time until, at some value of $\theta^*(\delta^*/(1-\delta^*))^{-\frac{1}{2}} \gtrsim 10^{-2}$, the vortex becomes unstable to a non-axisymmetric disturbance.

On figure 14 we have differentiated between those points for which $\delta^* > 0{\cdot}2$ (filled symbols) and those for which $\delta^* < 0{\cdot}2$ (open symbols). Both the first instability (circles) and any subsequent instability (triangles) are shown for each vortex. When $\delta^* > 0{\cdot}2$ we see that the vortices become unstable at similar values of $\theta(\delta/(1-\delta))^{-\frac{1}{2}}$. The critical value is a weak function of ϕ, decreasing from 0·04 at $\phi \approx 10^2$ to 0·01 at $\phi \approx 10^{10}$. On the other hand, those vortices with a very small depth ratio ($\delta^* < 0{\cdot}2$) can become unstable at much larger values of $\theta(\delta/(1-\delta))^{-\frac{1}{2}}$. This observation is consistent with the results for constant volume vortices (see figure 5), for which it was found that higher wavenumbers amplified at smaller values of δ when $\delta < 10^{-1}$. It was also concluded in that case (see § 3.2) that barotropic processes dominated the growth of disturbances at such small depth ratios. This, indeed, is the rationale for differentiating between instabilities of constant flux vortices at small and large depth ratios.

For instabilities at large depth ratios ($\delta^* > 0{\cdot}2$) the results are broadly consistent with those predicted by Phillips' model and the analyses of Hart (1972, 1980), in which there is no horizontal shear. The onset of baroclinic instability is known, however, to be dependent upon the velocity profile in the mean flow. The vortices appear to be 'less stable' at smaller values of ϕ and these are the conditions at which friction has had a greater influence on the motion in the vortex. A measure of the velocity profile at marginal stability is obtained from the radius R^* at instability non-dimensionalized by the viscous length scale R_ν.

The ratio R^*/R_ν is plotted against ϕ on figure 15. Apart from the radius at which instability was first observed (circles), the figure shows the radii at which the second (triangles) and third (squares) instabilities occurred. (A second instability is not shown for a number of the experiments because the source was sometimes turned off after a stable vortex had reformed. In other cases, the vortex reached the side walls before a second instability occurred). In two cases, the ratio R/R_ν is plotted for the observed axisymmetric flow (crosses) as the vortex grows. Figure 15 shows that R^*/R_ν is smaller at larger values of ϕ, and these are the conditions at which the inner inviscid core occupies a larger fraction of the vortex. Thus the influence of friction upon the velocity profile appears to destabilize the vortex.

Another observation which demonstrates the role of frictional effects is that our vortices rapidly become unstable once the source flow is turned off. Friction causes the radius to increase and the depth to decrease. The parameter $\theta(\delta/(1-\delta))^{-\frac{1}{2}}$ therefore rapidly decreases towards its critical value.

(iii) *The marginally unstable mode.* The experiments with a confined source of fluid involve flows that pass through a sequence of quasi-steady states in which the buoyancy, Coriolis and centrifugal forces are balanced. Thus a marginally stable state is approached slowly as the vortex grows and $\theta(\delta/(1-\delta))^{-\frac{1}{2}}$ decreases towards the critical value. As was noted in § 3.2, the lowest wavenumber that can release energy is $n = 2$. Hence (3.1) implies that this mode is the first to become unstable. Higher

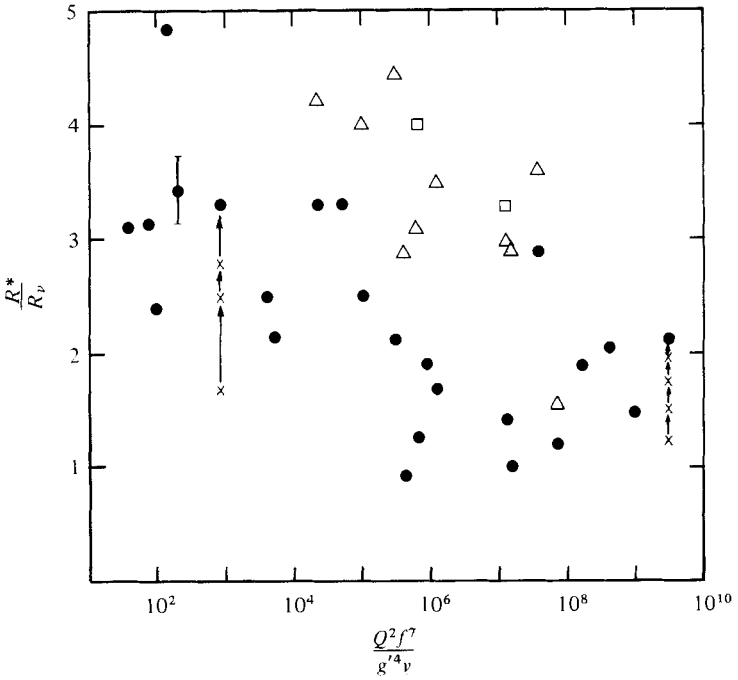

FIGURE 15. The critical radius of the vortex R^* non-dimensionalized by the viscous length scale R_ν as a function of $\phi = Q^2f^7/g'^4\nu$. Circles, triangles and squares denote the first, second and third instabilities, respectively. Two examples (marked by crosses) show the approach of a vortex towards its critical size. Typical error bars are shown.

wavenumbers require even smaller values of $\theta(\delta/(1-\delta))^{-\frac{1}{2}}$. A similar result was found by Hart (1972), except that he found the first mode to become unstable (for inviscid flow) had wavenumber $n = 1$. However, in his case the interface does not intersect either horizontal boundary so that this mode leads to a decrease of the potential energy of the flow.

In contrast to the experiments described in this section, the constant volume vortices discussed in § 3 collapse rapidly into a state of quasi-geostrophic balance with, in many cases, highly supercritical values of $\theta(\delta/(1-\delta))^{-\frac{1}{2}}$. Then the disturbance with the largest growth rate, given approximately by (3.3), dominates the pattern and higher wavenumbers are observed.

(iv) *Large-amplitude behaviour.* The evolution of the flow after a disturbance has grown to large amplitude depends on the depth ratio δ^*. It may also depend on the initial velocity profile (determined by R^*/R_ν), although probably to a lesser extent. As a vortex grows by the continuous addition of fluid, δ increases until $\theta(\delta/(1-\delta))^{-\frac{1}{2}}$ reaches a critical value. At this point non-axisymmetric disturbances lead to a rapid reduction of δ. If the vortex restabilizes, the depth ratio increases again until the critical value of $\theta(\delta/(1-\delta))^{-\frac{1}{2}}$ is reached and a second instability occurs. The radius of the vortex at the second instability is greater than at the first (see figure 15) and δ^* is larger. Consequently, the potential and kinetic energy of the vortex are greater at each successive instability.

For the constant volume vortices it was found that the strength of the cyclonic circulations produced by the instability increased with the depth ratio. The same is true of the constant flux vortices. Consequently, the strength of the cyclones increases

at each subsequent instability of a given vortex. Eventually they become sufficiently strong to cause the central anticyclonic vortex to split apart. Thus a vortex may re-stabilize after the first few instabilities but break up after a subsequent one.

The continuous inflow of source fluid supplies anticyclonic relative vorticity to the central vortex. Consequently, if the source is turned off, as in figure 10, then it should be easier for the cyclones to pull the central anticyclone apart. Indeed, we observe that the vortex can only re-stabilize if the source flow is maintained.

5. Intrusions into a density gradient

A brief description is given here of the flow that is produced by a continuous source of fluid in a linear density gradient. The vortex flow has many features in common with that in the two-layer experiments (§ 4). In particular, non-axisymmetric disturbances again appear when the vortex reaches a critical size and the nature of the subsequent break-up of the intrusion is identical.

These experiments were all performed in the rectangular tank described in § 2 with a fluid depth of 40 cm. A constant vertical density gradient was most easily produced by bringing two layers of salt solution into solid-body rotation, and then stirring vertically with a horizontal grid (which also rotated with the container). After a settling period of one hour, dye streaks revealed that no motion relative to the container remained. Salinity samples showed the density variation to be close to linear throughout a deep central portion of the fluid column. Another salt solution was then released at its own density level from the source described in § 4. In the absence of rotation the intruding fluid spread radially in a thin layer. In a rotating environment the intrusion formed an anticyclonic vortex round the source. For given fluid properties this system has only three adjustable parameters: the Coriolis parameter f, the (constant) flow-rate Q and the buoyancy frequency $N = (-(g/\rho)\,d\rho/dz)^{\frac{1}{2}}$.

Before discussing the onset of non-axisymmetric disturbances, we shall describe the basic axisymmetric flow. Figures 16(*a*) and (*b*) are shadowgraph images of two of the vortices. These vortices are axisymmetric, the azimuthal flow within them being circular and anticyclonic. There is also anticyclonic motion in the environment above and below the vortex due to the vertical compression of fluid columns as the vortex grows. The aspect ratio h/R, where h is the half-depth and R is the vortex radius, of these two vortices are quite different (0·47 and 0·99, respectively). However, the values of the Prandtl ratio Nh/fR are very similar (0·28 and 0·32, respectively). Gill (1981) presents an exact solution for a two-dimensional, inviscid intrusion. His model predicts that Nh/fR is a constant of order unity. The observation that the Prandtl ratio for the laboratory vortices is considerably smaller than the inviscid value indicates that viscosity is important. As in the two-layer case friction acts over the lifetime of a laboratory vortex, transferring angular momentum to the intruding fluid and flattening the density contours. The finite size of the source also contributes to this effect, as discussed in § 4.

In figures 16(*a*) and (*b*) a series of density steps is visible in the density gradient above and below the homogeneous intrusions. The number and horizontal extent of these structures grow with time. They are therefore more extensive, for a vortex of given volume, in experiments with smaller flow-rates Q (figure 16*a*). The layers appear to be identical to those that develop in a rotating salinity gradient adjacent to a more

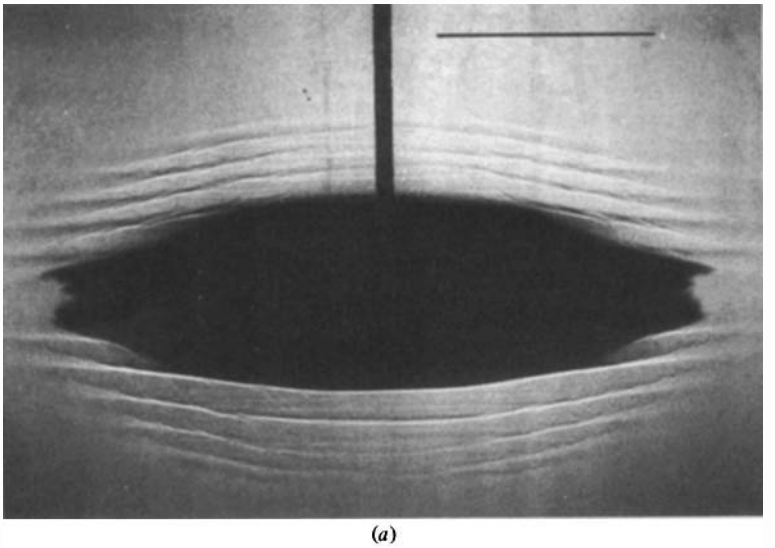

(*a*)

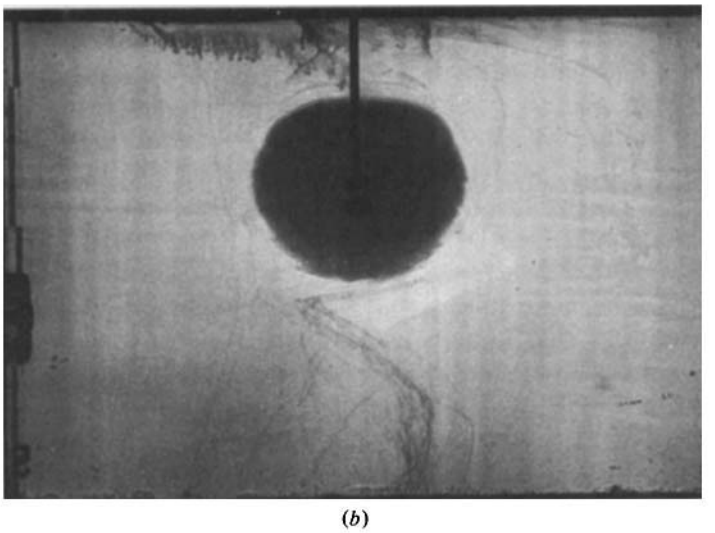

(*b*)

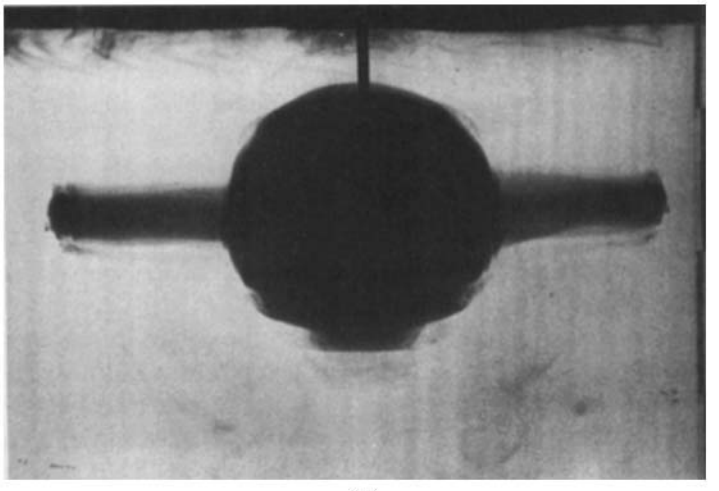

(*c*)

slowly rotating horizontal disk (Baker 1971, Calman 1977). In the present case, the solid disk is replaced by a domed density interface. The density steps are considered to be a finite-amplitude manifestation of a viscous-diffusive overturning proposed by McIntyre (1970). The presence of the layers appears to have no influence on the instability of the vortex, which will now be described.

The vortices in a linear density gradient become unstable and break up in the same manner as those at the free surface of a homogeneous layer. The intrusion increases in volume until the available energy is sufficient to amplify non-axisymmetric disturbances. As for the constant flux, two-layer vortices, the amplified mode always has an azimuthal wavenumber $n = 2$.

Again the $n = 1$ baroclinic mode cannot release potential energy as it corresponds to the motion of the vortex along its own density level which is a geopotential surface. Two 'spiral arms' originate from the crests of the perturbation, forming a cyclonic ring of source fluid on each side of the elongated anticyclonic vortex. This stage is shown in figure 16(*c*), which is a later stage of the vortex shown in figure 16(*b*) (the flow is viewed along the major axis of the elongated central vortex).

The half-depth h^* and radius R^* were measured immediately prior to the onset of instability of the vortex in three experiments. The critical Prandtl ratio Nh^*/fR^* took the values 0·28, 0·32 and 0·15, and so we conclude that $Nh^*/fR^* \lesssim 0{\cdot}2$ implies an unstable vortex. The flow eventually breaks up to form two pairs of stable vortices, each with larger values of the Prandtl ratio. The critical internal Richardson number in these experiments is $(Nh^*/f^*R^*)^2 \sim 0{\cdot}02$ to 0·1, a value that is comparable with $\theta^* \sim 0{\cdot}02$ for the two-layer experiments.

6. Conclusions

Some simple experiments demonstrate a number of important properties of unstable disturbances in a two-layer, rotating fluid. Using either a constant volume of fluid or a constant flux from a small source, the experiments produce basic axisymmetric flows of horizontal scale R, in which the density interface intersects one horizontal boundary. The two types of flow possess different velocity and potential vorticity profiles, but yield very similar behaviour of amplifying wavelike disturbances and subsequent non-axisymmetric motions.

The stability of both systems can be described by the two dimensionless parameters θ (the square of the ratio of the Rossby radius $(g'h)^{\frac{1}{2}}/f$ to the length scale R) and the depth ratio $\delta = h/H$. Vortices in the constant flux experiments pass from stable to marginally unstable conditions when $\theta(\delta/(1-\delta))^{-\frac{1}{2}} \sim 0{\cdot}02$. If the density interface intersects the free surface, the marginally unstable mode always has an azimuthal wavenumber $n = 2$. While the disturbance is growing we observe that its phase

FIGURE 16. Side-view shadowgraph images of vortices produced by a constant flux of (dyed) fluid from a small source in a constant density gradient. (*a*) $f = 1{\cdot}1\ \mathrm{s}^{-1}$, $N = 0{\cdot}66\ \mathrm{s}^{-1}$, $Q = 1{\cdot}3\ \mathrm{cm}^3\ \mathrm{s}^{-1}$ and $t = 780$ s after the source was turned on; (*b*) $f = 1{\cdot}1\ \mathrm{s}^{-1}$, $N = 0{\cdot}35\ \mathrm{s}^{-1}$, $Q = 4{\cdot}8\ \mathrm{cm}^3\ \mathrm{s}^{-1}$ and $t = 360$ s; (*c*) the same vortex as in (*b*) but at $t = 480$ s. The vortices in (*a*) and (*b*) are axisymmetric about the axis of rotation but in (*c*) we are looking along the major axis of a very elongated vortex. The line superimposed on the photograph in (*a*) is 10 cm long.

increases with depth (or with decreasing radius), and such a phase variation is a distinguishing feature of baroclinically unstable modes. Instability leads to a decrease of the depth of the vortex and therefore a release of potential energy. On the other hand, if the interface intersects the horizontal bottom boundary, the mode with $n = 1$ can be the first to become unstable, but this is a centrifugal instability due to the flat bottom which crosses geopotential surfaces. Vortices can also be unstable at values of $\theta(\delta/(1-\delta))^{-\frac{1}{2}}$ significantly greater than 0·02 when $\delta < 0{\cdot}2$, and this is thought to be due to the supply of kinetic energy from the lateral shear.

The constant volume experiments, on the other hand, produce supercritical flow. Again, the minimum wavenumber observed for those cases in which the density front intersects the free surface is $n = 2$. As θ_0 is decreased the wavenumber increases. However, as δ_0 is decreased from unity at a fixed value of θ_0 the wavenumber passes through a minimum at a ratio of layer depths $\delta \sim 10^{-1}$. The growth rate of disturbances, though difficult to estimate with the present experimental arrangement, decreases with decreasing depth ratio δ. These results are consistent with those predicted for an instability that is predominantly baroclinic when the maximum depth of the vortex exceeds $\frac{1}{10}$ of the total depth of fluid, but predominantly barotropic when $\delta \approx \delta_0 < 10^{-1}$.

Our results for surface vortices produced by the collapse of a cylinder of fluid differ from the results of similar experiments in which the density front intersects the bottom boundary (Saunders 1973). Stable vortices could be produced on the flat bottom but not at the free surface, and vortex wandering ($n = 1$) is observed only for bottom vortices. The drift velocity of the amplifying disturbances is in the direction of flow for bottom vortices but not measurably different from zero for surface vortices. Finally, transitions from one wavenumber to another (at $\delta_0 = 1$) for surface vortices occur at smaller values of θ_0. This last effect and the existence of stable bottom vortices probably result from the viscous decay of the long waves by the bottom Ekman layer. Vortex wandering depends upon the sign of the horizontal density gradient and the fact that the bottom boundary is not a geopotential surface. A variation of the drift velocity of regular baroclinic waves has also been observed in a differentially heated, rotating annulus (Douglas, Hide & Mason 1972) when the sign of the horizontal temperature gradient is reversed, or the free surface is replaced by a rigid lid.

The presence of a density front leads to dramatic large amplitude behaviour of the non-axisymmetric flow. In both types of experiment, pairing of vortices of opposite sign causes some or all of the fluid in the original anticyclonic vortex to be carried away in the radial direction. At sufficiently large values of the depth ratio δ, the first stage of pairing involves a primarily baroclinic disturbance that is unstable. As its amplitude grows there is an accumulation of cyclonic vorticity just ahead (in the cyclonic direction) of each crest of the disturbance. Numerical calculations (Orlanski 1969, Hart 1974) for a quasi-geostrophic current with horizontal shear show that mixed modes can be unstable when $\theta \sim O(1)$, with perturbations receiving both kinetic and potential energy. On the other hand, when the Rossby radius is much smaller than the horizontal length scale ($\theta \ll 1$) a primarily baroclinic instability can transfer kinetic energy into the mean flow. In our experiments there is a large cyclonic horizontal shear near the density interface, while $\theta \gtrsim 10^{-2}$. Thus at large depth ratios we are unable to say whether the kinetic energy of the intensifying cyclonic circulations

is drawn from the horizontal shear or from the release of potential energy by the baroclinic disturbance.

Once formed, the cyclones assist the release of potential energy from the density field by entraining into a cyclonic ring buoyant fluid from the original vortex. They also influence the formation of closed anticyclonic circulation within the baroclinic wave, and the splitting of the central vortex. Vortex dipole structures result and these propagate over the free surface.

At very small values of the depth ratio ($\delta < 10^{-1}$) our observations indicate that the initial perturbation is primarily barotropic. However, instability again leads to the release of potential energy stored in the original vortex. As the disturbance grows to large amplitude, vortex dipoles similar to those found at larger δ are formed, although they remove a smaller proportion of the fluid from the original vortex. A strong anticyclone remains after the vortex pairing and splitting process is complete.

All of our laboratory flows have Rossby numbers $\gtrsim 10^{-1}$, so that ageostrophic effects must be included in a full description of the fluid motion. Finite Rossby-number effects are also important near fronts in the atmosphere and ocean, where the depth of one layer approaches zero and the fluid vorticity can approach $-f$. The consequent stretching of fluid vortex lines has been shown (see Hoskins 1976) to produce an asymmetry in nonlinear baroclinic disturbances: the intensification of cyclonic vortices and weakening of anticyclonic vortices. It seems likely that such an asymmetry occurs in our experiments, particularly during the phase in which cyclonic circulation is intensifying and streamlines within the anticyclonic lobes are closing.

There are several ways in which this work could be extended. In particular, a better description of the basic axisymmetric flows, including the influence of friction and depth dependence, would enable a more satisfactory stability analysis to be carried out. The subsequent non-axisymmetric flow in the two-layer experiments also has a depth dependence that we have not fully investigated. For homogeneous vortices within a density gradient our observations show that the flow behaviour has much in common with that in the two-layer system. However, our examination of such intrusions is incomplete and their full description requires further study.

Much of this work has developed as a result of conversations with Professor J. S. Turner, and we are very grateful for his encouragement and advice. The rotating table was skilfully constructed by Mr D. Cheesley and Mr D. Lipman, and our thanks are due to Mr C. Chalk for his help with the photography. R. W. G. was supported by a grant from the Natural Environment Research Council.

REFERENCES

BAKER, D. J. 1971 Density gradients in a rotating stratified fluid: experimental evidence for a new instability. *Science* **172**, 1029–1031.

BARCILON, V. 1964 Role of the Ekman layers in the stability of the symmetric regime obtained in a rotating annulus. *J. Atmos. Sci.* **21**, 291–299.

BUSSE, F. H. 1968 Shear flow instability in rotating systems. *J. Fluid Mech.* **33**, 577–589.

CALMAN, J. 1977 Experiments on high Richardson number instability of a rotating stratified shear flow. *Dyn. Atmos. Oceans* **1**, 277–297.

CSANADY, C. T. 1979 The birth and death of a warm core ring. *J. Geophys. Res.* **84**, 777–780.

DOUGLAS, H. A., HIDE, R. & MASON, P. J. 1972 An investigation of the structure of baroclinic waves using three-level streak photography. *Quart. J. Roy. Met. Soc.* **98**, 247–263.

FLIERL, G. R. 1979 A simple model for the structure of warm and cold core rings. *J. Geophys. Res.* **84**, 781–785.

GILL, A. E. 1981 Homogeneous intrusions into a rotating stratified fluid. *J. Fluid Mech.* **103**, 275–295.

GILL, A.E., GREEN, J. S. A. & SIMMONS, A. J. 1974 Energy partition in the large-scale ocean circulation and the production of mid-ocean eddies. *Deep-Sea Res.* **21**, 499–528.

GILL, A. E., SMITH, J. M., CLEAVER, R. P., HIDE, R. & JONAS, P. R. 1979 The vortex created by mass transfer between layers of a rotating fluid. *Geophys. Astrophys. Fluid Dyn.* **12**, 195–200.

HART, J. E. 1972 A laboratory study of baroclinic instability. *Geophys. Fluid Dyn.* **3**, 181–209.

HART, J. E. 1974 On the mixed stability problem for quasi-geostrophic ocean currents. *J. Phys. Oceanogr.* **4**, 349–356.

HART, J. E. 1980 An experimental study of nonlinear baroclinic instability and mode selection in a large basin. *Dyn. Atmos. Oceans* **4**, 115–136.

HIDE, R. 1967 Detached shear layers in a rotating fluid. *J. Fluid Mech.* **29**, 39–60.

HOSKINS, B. J. 1976 Baroclinic waves and frontogenesis models. I. Introduction and Eady waves. *Quart. J. Roy. Met. Soc.* **102**, 103–122.

MCINTYRE, M. E. 1970 Diffusive destabilization of the baroclinic circular vortex. *Geophys. Fluid Dyn.* **1**, 19–57.

ORLANSKI, I. 1969 The influence of bottom topography on the stability of jets in a baroclinic fluid. *J. Atmos. Sci.* **26**, 1216–1332.

PEDLOSKY, J. 1976 On the dynamics of finite amplitude baroclinic waves as a function of supercriticality. *J. Fluid Mech.* **78**, 621–637.

PEDLOSKY, J. 1979 *Geophysical Fluid Dynamics*. Springer.

PHILLIPS, N. A. 1954 Energy transformations and meridional circulations associated with simple baroclinic waves in a two level quasi-geostrophic model. *Tellus* **6**, 273–86.

SAUNDERS, P. M. 1973 The instability of a baroclinic vortex. *J. Phys. Oceanogr.* **3**, 61–65.